Journal of Computational Physics (2024)

Contents lists available at ScienceDirect

Journal of Computational Physics

journal homepage: www.elsevier.com/locate/jcp

Conservative, bounded, and nonlinear discretization of the Cahn-Hilliard-Navier-Stokes equations

Jason Goulding[a], Tamar Shinar[a,*], Craig Schroeder[a,*]

[a]*Department of Computer Science and Engineering, University of California, Riverside, 351 Winston Chung Hall, Riverside, CA 92521-0429, USA*

ARTICLE INFO

Article history:

ABSTRACT

The Cahn-Hilliard equation describes phase separation in a binary mixture, typically modeled with a phase variable that represents the concentration of one phase or the concentration difference between the two phases. Though the system is energetically driven toward solutions within the physically meaningful range of the phase variable, numerical methods often struggle to maintain these bounds, leading to physically invalid quantities and numerical difficulties. In this work, we introduce a novel splitting and discretization for the Cahn-Hilliard equation, coupled with the Navier-Stokes equations, which inherently preserves the bounds of the phase variable. This approach transforms the fourth-order Cahn-Hilliard equation into a second-order Helmholtz equation and a second-order nonlinear equation with implicit energy barriers, which is reformulated and solved with a safeguarded optimization-based solution method. Our scheme ensures the phase variable remains in the valid range, robustly handles large density ratios, conserves mass and momentum, maintains consistency between these quantities, and achieves second-order accuracy. We demonstrate the method's effectiveness through a variety of studies of two-dimensional, two-phase fluid mixtures.

1. Introduction

The Cahn-Hilliard equation describes the separation of a binary fluid mixture into domains that are pure in each phase [10, 20]. The mixture is typically modeled with a phase variable γ that represents the concentration of one phase ($\gamma \in [0, 1]$) or the concentration difference between the two phases ($\gamma \in [-1, 1]$). A variety of schemes have been developed for the numerical solution of the Cahn-Hilliard equation, including Fourier spectral methods [55, 32, 41], finite difference methods [26, 43, 30, 12, 36], and finite element methods [21, 9, 7, 24, 52, 31]. Though the system is

*Corresponding authors: email: shinar@cs.ucr.edu, craigs@cs.ucr.edu

energetically driven toward solutions within the physically meaningful range of γ, numerical methods for the solution of the Cahn-Hilliard equation may generate values outside this range, leading to physically invalid quantities and numerical difficulties [27, 35, 37]. Specifically, the phase variable is used to compute effective densities and viscosities. Under large density ratios, even a small excursion outside the valid range of values for γ can result in negative effective densities, and hence ill-posedness of the viscous momentum equation and loss of positive-definiteness in numerical solvers.

To model two-phase incompressible flows, the Cahn-Hilliard equation is coupled to the incompressible Navier-Stokes equations. Several works have investigated variants of this system, including the case of matched densities [33, 4], the Boussinesq approximation [38, 45, 3], and the more general Cahn-Hilliard-Navier-Stokes (CHNS) equations with varying densities and viscosities [51, 50, 40, 16, 19, 30, 36, 27].

Cahn-Hilliard models vary based on the choice of potential and mobility functions, and this impacts the theoretical boundedness properties of the phase variable. A common approach is to use the Ginzburg-Landau double-well polynomial potential with constant mobility [25, 36, 27], suitable for situations where the diffusion is not strongly dependent on the concentration field. This model permits the phase variable to go outside physically meaningful bounds. The Cahn-Hilliard model with concentration-dependent degenerate mobility, which is zero in pure phases, has also been widely used [7]. In this form, given initial data that satisfies the physical bounds, the solution has been shown to maintain the bounds [22]. Another commonly employed model uses a logarithmic potential based on the Flory-Huggins theory of polymer solutions [1, 11, 5]. The potential is singular with infinite energy barriers at the pure concentrations $\gamma = 0$ or $\gamma = 1$, preventing the solution from attaining or exceeding these values. This formulation admits a maximum principle so that the analytic solution remains within bounds [15, 47, 1].

Preserving the physical bounds of the phase variable in numerical solutions can be challenging even in models that admit a maximum principle. This requirement may also impose additional time step restrictions [14, 6, 48]. There have been many works aimed at developing bounds-preserving numerical methods. Several methods have addressed the issue of keeping γ in its physical bounds by using combinations of flux and slope limiters [25, 44]. Another approach to maintain the bounds of the phase variable is to explicitly clamp the variable in regions that exceed the bounds [18]. However, in order to conserve mass, the clipped mass must then be redistributed in a bounds-respecting manner. Chiu and Lin [13] applied such a strategy, uniformly distributing the clipped mass in the interfacial transition region. Huang et al. [35] proposed a boundedness mapping, a volume redistribution scheme that maintains the phase variable in the physical range. This method determines a set of conservative fluxes that maintain the global mass of the system while distributing mass from regions that undershoot or overshoot. This method was used to maintain bounds in the simulation of the Cahn-Hilliard-Navier-Stokes equations in both [36] and [27]. One drawback of the approach is that the choice of mass redistribution is controlled by a weight function and the determination of the fluxes requires a computationally expensive Poisson equation solve. The boundedness mapping approach was further developed in [37] for the more challenging case of multiphase flows with three or more phases.

When modeled with a singular logarithmic potential, numerical methods for the Cahn-Hilliard equation must be carefully designed to maintain the solution strictly within the physical bounds. Copetti and Elliott [14] developed a

piecewise linear finite element scheme with backward Euler time discretization for the Cahn-Hilliard equation with a logarithmic free energy and gave conditions on the time step and initial data to ensure boundedness of the solution. Barrett and Blowey [6] further proved error bounds for this scheme. Yang and Zhao [53] developed an unconditionally energy-stable scheme for the CH equation with logarithmic potential that is linear and symmetric positive definite.

Based on the work of Eyre [23], several approaches utilize convex splitting, where the potential is expressed as a difference of convex functions and a convex nonlinear subproblem is formulated and solved implicitly to maintain the solution bounds. Li et al. [42] proposed an unconditionally stable nonlinear scheme based on convex splitting of the potential and solved by Newton iteration. The convergence of the scheme was analyzed in [17] by converting the problem into a convex minimization. Also based on a convex splitting of the potential and implicit treatment of the logarithmic terms, Chen et al. [11] developed first and second order finite difference schemes where the positivity of the logarithmic argument is maintained without incurring an additional time step restriction.

Bailo et al. [5] used a convex splitting approach combined with an upwind methodology for discretization of the mobility to construct a semi-implicit scheme that unconditionally maintains the boundedness of the phase variable. Acosta-Soba et al. [2] also pursued an upwind methodology for both the flow velocity and the mobility in a discontinuous Galerkin scheme for the convective Cahn-Hilliard equation with polynomial potential and degenerate mobility, maintaining the bounds on the solution. A bounds-preserving upwind scheme was also developed in [34].

In this work, we introduce a novel splitting for the numerical solution of the Cahn-Hilliard-Navier-Stokes equations that maintains the phase variable $\gamma \in [0, 1]$ by construction. We use a piecewise potential approximation with logarithmic terms singular at the pure phases. Similar to convex splitting approaches, our method results in a nonlinear equation implicit in the phase variable that maintains boundedness of the solution. We reformulate the nonlinear equation as a convex optimization facilitating solution through a safeguarded optimization-based scheme. Existing approaches enforce the bounds constraint on γ by using a barrier energy, preventing γ from leaving the feasible region by requiring infinite energy to do so. Barriers of this type lead to poorly-conditioned numerical problems. We instead enforce the constraint $0 \leq \gamma \leq 1$ by construction, computing γ as the output of a function that cannot produce a value outside of the feasible range. Practically, this has the effect of moving our energy barrier energy out to infinity, resulting in an energy that grows slowly and is well-behaved everywhere. The resulting method is observed to be second order accurate and can robustly simulate large density ratios. We demonstrate the method's effectiveness through a variety of studies of two-dimensional, two-phase fluid mixtures.

2. Governing equations

2.1. Cahn-Hilliard equation

The Cahn-Hilliard equations can be expressed as

$$\frac{\partial \gamma}{\partial t} + \nabla \cdot (\mathbf{u}\gamma) = \nabla \cdot (M \nabla \xi) + S_\gamma \tag{1}$$

$$\xi = \lambda (F'(\gamma) - \nabla^2 \gamma) \tag{2}$$

$$\lambda = \frac{3}{2\sqrt{2}} \sigma \eta. \tag{3}$$

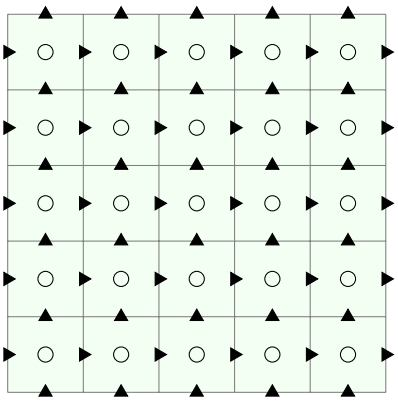

Fig. 1: The MAC grid stores γ and pressure on cell centers (circles). Velocties are stored by component on faces (represented by triangles), (Reproduced from [27].)

We label the two fluid phases as 0 and 1. The volume fraction of fluid 1 is represented as the phase-field function $\gamma \in [0, 1]$. The chemical potential is ξ. λ, called the mixing energy density in Huang et al. [35], is a parameter that incorporates the surface tension constant σ and η, a parameter which influences the width of the phase transition region. $\mathbf{u}$ is the fluid velocity, M is the mobility, S_γ is an external source term, and F is a double well potential function. The details of F and its corresponding derivative F' are described in Section 3.1.2.

The properties of fluid phases 0 and 1 are density (ρ_0, ρ_1) and viscosity (μ_0, μ_1) respectively. For a given location $\mathbf{x}$, we compute the effective density and viscosity of the phase mixture with

$$\rho(\mathbf{x}) = \rho_0 + (\rho_1 - \rho_0)\,\gamma(\mathbf{x}) \tag{4}$$

$$\mu(\mathbf{x}) = \mu_0 + (\mu_1 - \mu_0)\,\gamma(\mathbf{x}). \tag{5}$$

2.2. Navier-Stokes equations

The Navier-Stokes equations for incompressible flow are given by

$$\frac{\partial \rho}{\partial t} + \nabla \cdot \mathbf{m} = S_m \tag{6}$$

$$\nabla \cdot \mathbf{u} = 0 \tag{7}$$

$$\frac{\partial(\rho \mathbf{u})}{\partial t} + \nabla \cdot (\mathbf{m} \otimes \mathbf{u}) = -\nabla p + \nabla \cdot (\mu(\nabla \mathbf{u} + (\nabla \mathbf{u})^T)) + \rho g + \sigma \kappa \nabla(h(\gamma)) + S_{\mathbf{u}}, \tag{8}$$

where ρ is the effective density, $\mathbf{m}$ is the mass flux consistent with the γ evolution (1) [36], S_m is an external mass source, $\mathbf{u}$ is the velocity, p is the pressure, μ is the effective viscosity, g is the acceleration of gravity, σ is the coefficient of surface tension, κ is the interface curvature, $h(\gamma)$ is a regularized Heaviside function as defined in [27], and $S_{\mathbf{u}}$ is the external momentum source.

3. Discretizations

In this section we describe the temporal and spatial discretizations of the Cahn-Hilliard and Navier-Stokes equations. As in [27], we use a uniform MAC grid (Figure 1) with γ and pressure stored at cell centers. Velocities are split by components and stored on cell faces. Unless otherwise specified, we use the same discretizations as in [27].

3.1. Cahn-Hilliard equation

Goulding et al. [27] introduced a discretization that was simple and effective, but it did not ensure $\gamma \in [0, 1]$. Instead, they used the bounds-enforcing scheme introduced in Huang et al. [35] to correct gamma in a postprocess. That postprocess is non-local, which is undesirable since mass conservation is a local conservation property. It also requires a Poisson solve to determine associated conservative fluxes which incurs significant computational cost [27]. In this work, we construct a scheme that automatically guarantees $\gamma \in (0, 1)$ without the need for any postprocessing steps. We do this by formulating F with a barrier at 0 and 1 (much as some existing formulations of F do [10]) and treating the term $F'(\gamma^{n+1})$ implicitly.

3.1.1. Scheme derivation

We begin our formulation of our scheme with the scheme from [27] where the fourth order Cahn-Hilliard equation is split into two second-order Helmholtz equations as

$$A - s\widehat{\Delta t}\nabla^2 A = \gamma^* + B + \widehat{\Delta t} S_\gamma^{n+1} \tag{9}$$

$$\gamma^{n+1} - s\widehat{\Delta t}\nabla^2 \gamma^{n+1} = A - B, \tag{10}$$

where γ^* is the result of advecting γ^n. In the absence of source terms, the scheme should be discretely mass conserving, requiring

$$\int_\Omega \gamma^{n+1}\, dV = \int_\Omega \gamma^n\, dV \tag{11}$$

Note that by the divergence theorem, any field B with zero flux or periodic boundary conditions satisfies

$$\int_\Omega \nabla^2 B\, dV = 0, \tag{12}$$

so that Laplacian terms do not contribute to mass conservation. Therefore, assuming $S_\gamma^{n+1} = 0$ and integrating equations (9) and (10), we get

$$\int_\Omega A\, dV = \int_\Omega \gamma^*\, dV + \int_\Omega B\, dV \tag{13}$$

$$\int_\Omega \gamma^{n+1}\, dV = \int_\Omega A\, dV - \int_\Omega B\, dV \tag{14}$$

$$= \int_\Omega \gamma^*\, dV = \int_\Omega \gamma^n\, dV, \tag{15}$$

where the last equality comes from assuming conservative advection. Observe that the contents of B do not matter, since it is added before solving a Helmholtz equation and subtracted off afterwards. As a useful rule, terms that are not Laplacians must be added and subtracted in this way to achieve conservation.

Next we turn to the general form we want for our scheme. Schemes such as [36] also include $\nabla^2 F'(\gamma)$ terms, which we allow in our scheme as well. We also use γ^{AB}, described below, as an explicit estimate of γ^{n+1}. This leads to a potential general scheme of the form

$$A + a_1\nabla^2 A = \gamma^* + a_2\gamma^{AB} + a_3\nabla^2 F'(\gamma^{AB}) + a_4 F'(\gamma^{AB}) \tag{16}$$

$$\gamma^{n+1} + c_1\nabla^2\gamma^{n+1} = A + c_2\gamma^{AB} + c_3\nabla^2 F'(\gamma^{AB}) + c_4 F'(\gamma^{AB}) + c_5 F'(\gamma^{n+1}), \tag{17}$$

which adds in the necessary implicit treatment of F' but fails to be conservative since the $F'(\gamma^{n+1})$ term is not canceled (unless $c_5 = 0$, which would then not be implicit). To restore conservation, we need to cancel out the implicit term, which suggests a scheme of the form

$$A + a_1\nabla^2 A = \gamma^* + a_2\gamma^{AB} + a_3\nabla^2 F'(\gamma^{AB}) + a_4 F'(\gamma^{AB}) \tag{18}$$

$$C + c_1\nabla^2 C = A + c_2\gamma^{AB} + c_3\nabla^2 F'(\gamma^{AB}) + c_4 F'(\gamma^{AB}) + c_5 F'(\gamma^{n+1}) \tag{19}$$

$$\gamma^{n+1} = C + g_2\gamma^{AB} + g_3\nabla^2 F'(\gamma^{AB}) + g_4 F'(\gamma^{AB}) + g_5 F'(\gamma^{n+1}), \tag{20}$$

which will be conservative provided $a_2 + c_2 + g_2 = 0$, $a_4 + c_4 + g_4 = 0$, and $c_5 + g_5 = 0$. Schemes of this form exist, but the $F'(\gamma^{AB})$ terms are problematic, since $F(\gamma)$ has barriers at 0 and 1 but γ^{AB} need not lie within this range. Instead, we replace them with $F'(\gamma)^{AB} = 2F'(\gamma^n) - F'(\gamma^{n-1})$, which is safe to compute since $0 < \gamma^n < 1$ will always be bounded. This suggests we should look for a scheme of the form

$$A + a_1\nabla^2 A = \gamma^* + a_2\gamma^{AB} + a_3\nabla^2 F'(\gamma)^{AB} + a_4 F'(\gamma)^{AB} \tag{21}$$

$$C + c_1\nabla^2 C = A + c_2\gamma^{AB} + c_3\nabla^2 F'(\gamma)^{AB} + c_4 F'(\gamma)^{AB} + c_5 F'(\gamma^{n+1}) \tag{22}$$

$$\gamma^{n+1} = C + g_2\gamma^{AB} + g_3\nabla^2 F'(\gamma)^{AB} + g_4 F'(\gamma)^{AB} + g_5 F'(\gamma^{n+1}) \tag{23}$$

subject to the constraints on the coefficients needed for conservation.

What remains is to select coefficients such that the scheme is consistent and formally 1.5 order accurate. We also prefer to discard terms from (23) where possible. Performing the truncation analysis leads to the scheme

$$A - s\widehat{\Delta t}\nabla^2 A = \gamma^* - 2\gamma^{AB} + \widehat{\Delta t} M\lambda\nabla^2 F'(\gamma)^{AB} \tag{24}$$

$$C - s\widehat{\Delta t}\nabla^2 C = A + 2\gamma^{AB} - bs\widehat{\Delta t}^2\nabla^2 F'(\gamma)^{AB} + b\widehat{\Delta t} F'(\gamma^{n+1}) \tag{25}$$

$$\gamma^{n+1} = C - b\widehat{\Delta t} F'(\gamma^{n+1}), \tag{26}$$

where $s = \sqrt{\frac{M\lambda}{\widehat{\Delta t}}}$ and $\widehat{\Delta t} = \frac{2}{3}\Delta t$. This scheme is consistent for any constant b. We examine restrictions on this constant in Section 3.1.2. We show that the method is consistent and order 1.5 accurate in Section 3.1.3.

3.1.2. Avoiding nested solves

We will solve (25) using Newton's method. Observe that for each Newton iteration, we must solve (26), which is a pointwise nonlinear equation. To stabilize Newton's method, we would like to formulate it as an optimization problem so that line searches can be employed. This requires us to integrate (25) with respect to C to form the objective, so that the optimality conditions recover (25). If we let $\gamma^{n+1} = f(C)$ denote the process of solving (26), then forming the objective requires us to integrate the function f. If f is obtained as that output of a numerical procedure, then computing this integral would be problematic. To have a practical chance of computing this integral, we will need a closed-form solution for f. Let g be the integral so that $\gamma^{n+1} = g'(C)$.

For most choices of the double-well potential F, the function $g'(C)$ will not be solvable in closed form. We must therefore restrict the form of F in such a way that it has the correct qualitative form while allowing g' to be computed

and integrated in closed form. We note that this is possible for two special forms. If $F(x)$ is a cubic polynomial, then

$$F(x) = a_3x^3 + a_2x^2 + a_1x + a_0 \tag{27}$$

$$\gamma = C - b\widehat{\Delta t}F'(\gamma) = C - b\widehat{\Delta t}(3a_3\gamma^2 + 2a_2\gamma + a_1), \tag{28}$$

which leads to a quadratic equation in γ that can be solved in closed form. Further, the quadratic equation for γ takes the general form $\gamma = g'(C) = k_0 + \sqrt{k_1 + k_2C}$, which can be integrated in closed form. Another form for F with this property is

$$F(x) = a_2x^2 + a_1x + a_0 + a_3\ln(x) \tag{29}$$

$$\gamma = C - b\widehat{\Delta t}F'(\gamma) = C - b\widehat{\Delta t}(2a_2\gamma + a_1 + a_3\gamma^{-1}). \tag{30}$$

Clearing the fractions leads to another quadratic equation in γ, this time of the form $\gamma = g'(C) = (k_0C + k_1) + \sqrt{(k_0C + k_1)^2 + k_2}$, which can also be integrated in closed form. (29) is notable in that it has a barrier at 0.

A suitable formulation of F must be a double-well energy function with barriers at 0 and 1. Neither form above has these properties, but a suitable function F can be constructed by combining energy terms of these forms piecewise. We note that piecewise formulations for F have been employed before [8, 28, 54]. It is clear that two logarithmic pieces will be required to get the necessary barriers. In addition, two cubic pieces are used to complete the double-well profile. We are thus looking for a potential of the form

$$F(\gamma) = \begin{cases} F_0(\gamma) & 0 \le \gamma \le r \\ F_1(\gamma) & r < \gamma < \frac{1}{2} \\ F_1(1-\gamma) & \frac{1}{2} < \gamma \le 1 - r \\ F_0(1-\gamma) & 1 - r < \gamma \le 1 \end{cases} \tag{31}$$

$$F_0(\gamma) = b_2x^2 + b_1x + b_0 + b_3\ln(x) \tag{32}$$

$$F_1(\gamma) = a_3x^3 + a_2x^2 + a_1x + a_0 \tag{33}$$

where we have assumed the symmetry $F(\gamma) = F(1-\gamma)$.

When solving the equation $\gamma = C - b\widehat{\Delta t}F'(\gamma)$, there is an additional complication. The piecewise boundaries of $F'(\gamma)$ are in terms of γ, not C. The corresponding boundaries for C could of course be computed by substituting boundary values for γ and solving for C, but we instead pursue a simpler strategy. We note that the double-well potential F will have two minima and a maximum. If we place the minima of F at r and $1-r$ and the maximum at $\frac{1}{2}$, then $F'(r) = F'(\frac{1}{2}) = F'(1-r) = 0$. If γ is one of these values, then $\gamma = C - b\widehat{\Delta t}F'(\gamma) = C$, so that the piecewise boundaries for γ and C are the same.

The piecewise formulation for F has eight degrees of freedom. Enforcing C^2 continuity eliminates four degrees of freedom. Placing a minimum at r and shifting the minimum to zero (i.e., $F'(r) = F(r) = 0$) eliminates two more. We only need to construct $F(\gamma)$ up to a global scale (we will scale it appropriately later), which eliminates one more. We are left with one more degree of freedom, so we choose to enforce C^3 continuity at r. We are now left with

$$F_0(\gamma) = 3(\gamma - r)(8r^2 - 4r\gamma - r + \gamma) - 12r^3\ln\frac{\gamma}{r} \qquad F_1(\gamma) = (r-\gamma)^2(3 - 2r - 4\gamma). \tag{34}$$

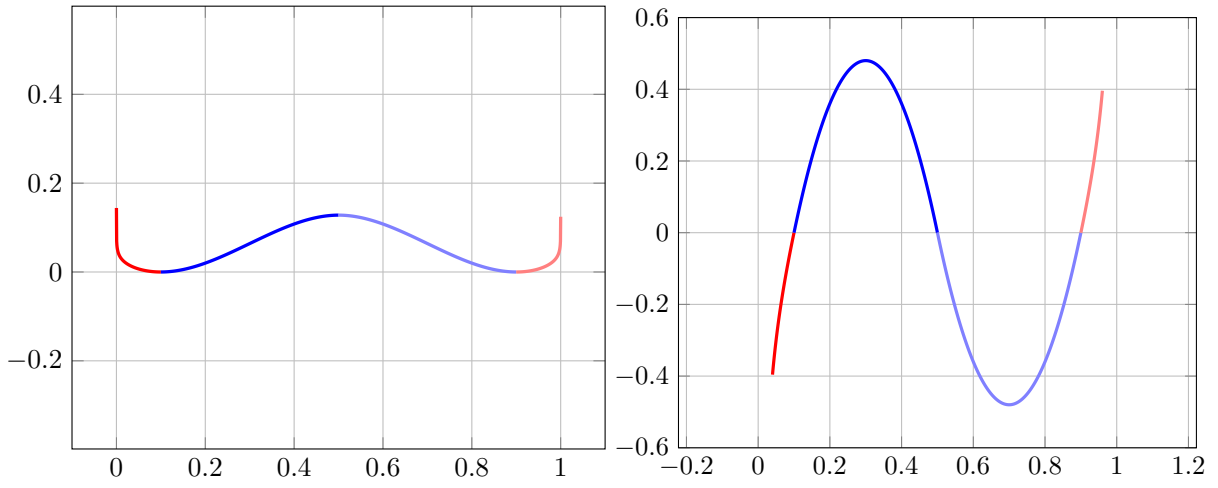

Fig. 2: Plots of $F(C)$ (left) and $F'(C)$ (right) corresponding to $q = 0.5$ and $r = 0.1$.

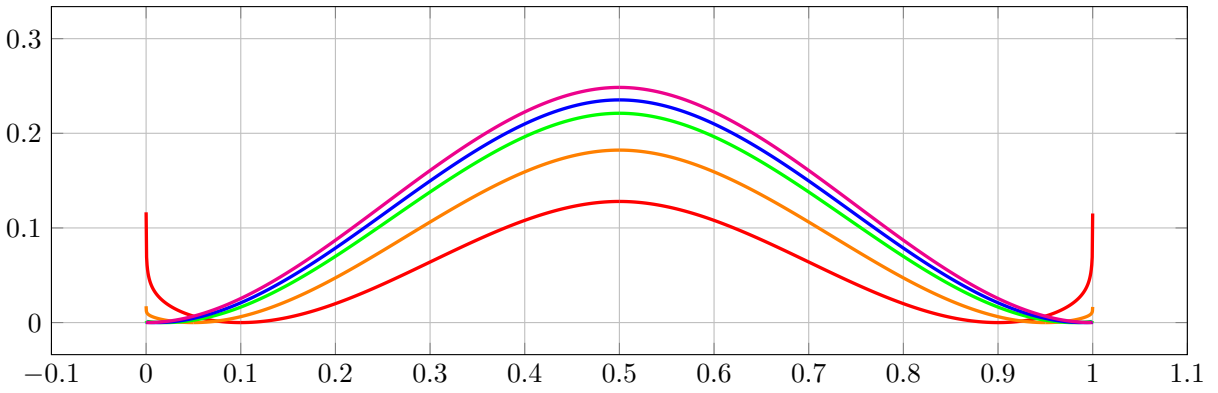

Fig. 3: Plot of $F(C)$ for different values of r: 0.1 (—), 0.05 (—), 0.02 (—), 0.01 (—), and 0.001 (—). The potential function converges pointwise in the limit $r \to 0$ over the range $0 < C < 1$.

Figure 2 shows a plot of $F(\gamma)$ and $F'(\gamma)$. Besides a global scale, this potential is also a function of the parameter r, which specifies the location of the minima. The dependence of this potential on r can be seen in Figure 3. The potential converges in the limit $r \to 0$, which allows our scheme to be run with r very nearly zero. This is important, since in regions far from the interface, γ will be comparable to r or $1 - r$.

The function $\gamma = g'(C)$ is defined as the solution of $\gamma = C - kF'(\gamma)$, where in the scheme we have the constant $k = b\widehat{\Delta t}$. The global scaling on F is absorbed into the constant b. g' can be expressed in closed form as

$$g'(C) = \begin{cases} g_0'(C) & 0 \le C \le r \\ g_1'(C) & r < C < \frac{1}{2} \\ 1 - g_1'(1-C) & \frac{1}{2} < C \le 1 - r \\ 1 - g_0'(1-C) & 1 - r < C \le 1 \end{cases} \tag{35}$$

$$q = 6k(1-2r) \qquad p = 1 + 6k(1-4r) \qquad s = 6r(1-6r)k \tag{36}$$

$$g_0'(C) = \frac{1}{2p} h_0'(C+s) \qquad h_0'(x) = x + \sqrt{x^2+L} = -\frac{L}{x - \sqrt{x^2+L}} \qquad L = 48kr^3p \tag{37}$$

$$g_1'(C) = \frac{1}{2} + h_1'\left(\frac{C-\frac{1}{2}}{12k}\right) \qquad h_1'(x) = K - \sqrt{K^2-x} = \frac{x}{K + \sqrt{K^2-x}} \qquad K = \frac{1-q}{24k} \tag{38}$$

We note that the first form of h_0' and h_1' is convenient for differentiation and integration, but the second form is more numerically robust since $x > 0$ and $K > 0$. In addition to $g'(C)$, which is used to compute γ^{n+1}, we also need g (for the optimization objective) and g'' (for the Hessian of the objective). The derivative g'' is straightforward

$$g''(C) = \begin{cases} g_0''(C) & 0 \le C \le r \\ g_1''(C) & r < C < \frac{1}{2} \\ g_1''(1-C) & \frac{1}{2} < C \le 1-r \\ g_0''(1-C) & 1-r < C \le 1 \end{cases} \tag{39}$$

$$g_0''(C) = \frac{1}{2p} h_0''(C+s) \qquad h_0''(x) = 1 + \frac{x}{\sqrt{x^2+L}} \qquad g_1''(C) = \frac{1}{12k} h_1''\left(\frac{C-\frac{1}{2}}{12k}\right) \qquad h_1''(x) = \frac{1}{2\sqrt{K^2-x}} \tag{40}$$

When computing the integral, we must be careful to ensure continuity.

$$g(C) = \begin{cases} g_0(C) - g_0(r) + g_1(r) & 0 \le C \le r \\ g_1(C) & r < C < \frac{1}{2} \\ C - \frac{1}{2} + g_1(1-C) & \frac{1}{2} < C \le 1-r \\ C - \frac{1}{2} + g_0(1-C) - g_0(r) + g_1(r) & 1-r < C \le 1 \end{cases} \tag{41}$$

$$g_0(C) = \frac{1}{2p} h_0(C+s) \qquad h_0(x) = \frac{x}{2} h_0'(x) + \frac{L}{2} \ln\left(h_0'(x)\right) \tag{42}$$

$$g_1(C) = \frac{C}{2} + 12k h_1\left(\frac{C-\frac{1}{2}}{12k}\right) \qquad h_1(x) = Kx + \frac{2}{3}(K^2-x)^{3/2} \tag{43}$$

In addition to r, the function g' also depends on k. The influence of this parameter is easier to understand in terms of the related quantity q, as seen in Figure 4. In the limit $q \to 0$, $\gamma \to C$ when $0 < C < 1$, with γ clamped to 0 or 1 outside this interval. In the limit $q \to 1$, we have $g'(\frac{1}{2}) \to \infty$. For $q > 1$ the relationship $C = \gamma + kF'(\gamma)$ ceases to be monotonic, so that its inverse g' does not exist as a continuous function. For the proposed scheme to exist, we must have $0 < q < 1$. While q is always positive, the requirement $q < 1$ effectively imposes a time step restriction. Figure 5 shows plots of $g(C)$ and $g''(C)$. Note that $g''(C)$ is continuous and positive (from (39) and (40)), which improves the conditioning of the optimization problem.

3.1.3. Temporal discretization

Our strategy for enforcing bounds on γ revolves around it ultimately being computed as $\gamma = g(C)$, where the function $g(C)$ must be chosen to never produce a value outside the range $0 \le \gamma \le 1$. This requires our time integration scheme to take a very specific form. In Section 3.1.1, we motivated this general form and then selected a specific scheme of this form that satisfied all of our requirements. In Section 3.1.2, we constructed a potential energy function $F(\gamma)$ that leads to a function $g(C)$ with suitable properties. With this, we have our completed scheme. In this section,

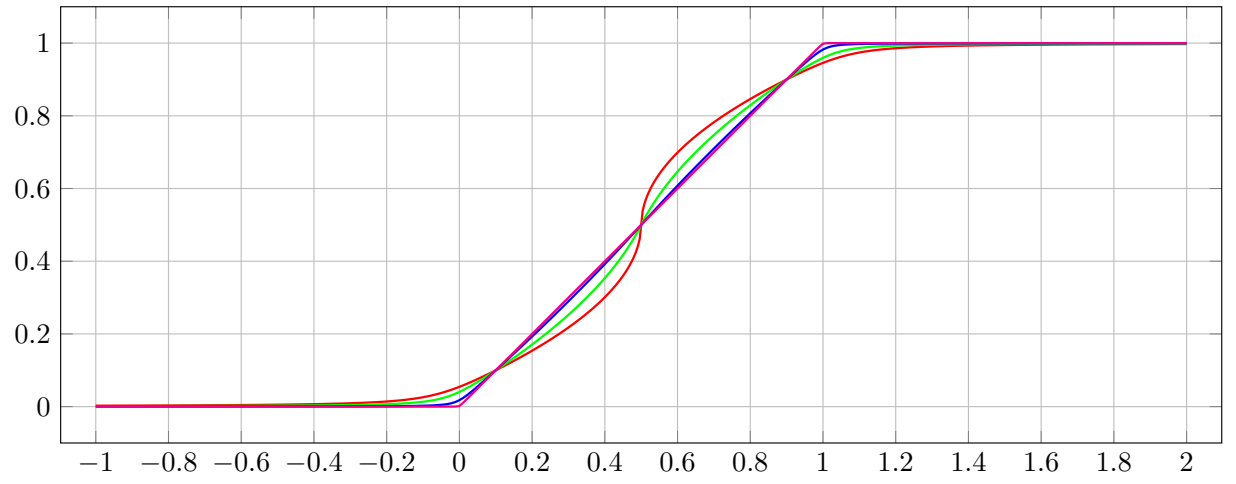

Fig. 4: Plot of $g'(C)$ for different values of q: 0.99 (—), 0.9 (—), 0.5 (—), 0.001 (—). The function g' converges to piecewise-linear in the limit $q \to 0$ and develops an infinite slope at $C = \frac{1}{2}$ in the limit $q \to 1$. When $q > 1$, (26), when viewed as a function $C(\gamma)$, is not monotonic. In this case, g' would become multivalued. Useful values of q are thus restricted to $0 < q < 1$ to ensure that (26) has a unique and continuous solution.

we rederive our scheme algebraically in order to show that it is consistent and has formal convergence order 1.5. As with similar methods that are formally 1.5 order accurate, we observe second order convergence in our numerical tests [36, 27].

We begin by combining (1) and (2) to get the form of the Cahn-Hilliard equation that we wish to discretize:

$$\frac{\partial \gamma}{\partial t} + \nabla \cdot (\mathbf{u}\gamma) = M\lambda\nabla^2(F'(\gamma) - \nabla^2\gamma) + S_\gamma. \tag{44}$$

As in Goulding et al. [27], we discretize the time derivative using the second-order scheme $\frac{\alpha\gamma^{n+1} - \alpha\gamma^{BD}}{\Delta t}$ with $\alpha = \frac{3}{2}$ and $\gamma^{BD} = \frac{4}{3}\gamma^n - \frac{1}{3}\gamma^{n-1}$. For the first time step we use a first-order single-step scheme with $\alpha = 1$ and $\gamma^{BD} = \gamma^n$. Explicit quantities for $\mathbf{u}$ and γ are discretized using an Adams-Bashforth scheme, where $\gamma^{AB} = \gamma^n$, $\mathbf{u}^{AB} = \mathbf{u}^n$ in the first step and $\gamma^{AB} = 2\gamma^n - \gamma^{n-1}$, $\mathbf{u}^{AB} = 2\mathbf{u}^n - \mathbf{u}^{n-1}$ in subsequent steps. We let $\widehat{\Delta t} = \Delta t/\alpha$, as α and Δt always occur together in practice.

Next, we derive the scheme presented in Section 3.1 directly from Equation (44). We begin with temporal discretization choices for γ and $\mathbf{u}$,

$$\frac{\gamma^{n+1} - \gamma^{BD}}{\widehat{\Delta t}} + \nabla \cdot \left(\mathbf{u}^{AB}\gamma^{AB}\right) = M\lambda\nabla^2\left(F'\left(\gamma^{n+1}\right) - \nabla^2\gamma^{n+1}\right) + S_\gamma^{n+1}. \tag{45}$$

Next we split out the advection term as an update from γ^{BD} to an intermediate quantity γ^*:

$$\frac{\gamma^* - \gamma^{BD}}{\widehat{\Delta t}} + \nabla \cdot \left(\mathbf{u}^{AB}\gamma^{AB}\right) = 0 \tag{46}$$

$$\frac{\gamma^{n+1} - \gamma^*}{\widehat{\Delta t}} = M\lambda\nabla^2\left(F'\left(\gamma^{n+1}\right) - \nabla^2\gamma^{n+1}\right) + S_\gamma^{n+1}. \tag{47}$$

Expanding on Shen and Yang [51] and Goulding et al. [27], we define s so that $s^2\widehat{\Delta t} = M\lambda$ and introduce extra terms (denoted T_1, T_2, and T_3) to facilitate the further splitting of the equation. Each term introduces a small error but

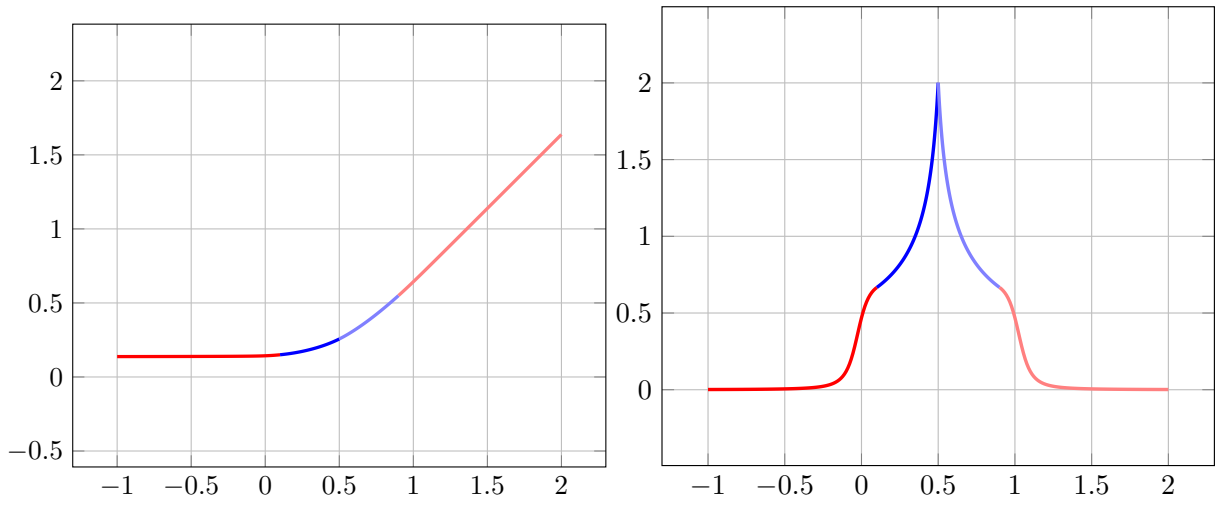

Fig. 5: Plots of $g(C)$ (left) and $g''(C)$ (right) corresponding to $q = 0.5$ and $r = 0.1$.

decreases rapidly under refinement (noting $s = O(\Delta t^{-0.5})$ and $k = O(\Delta t)$, with M and λ fixed):

$$T_1 = 2s(\gamma^{n+1} - \gamma^{AB}) = O(\Delta t^{1.5}) \tag{48}$$

$$T_2 = -M\lambda k\nabla^2\left(F'(\gamma^{n+1}) - F'(\gamma)^{AB}\right) = O(\Delta t^3) \tag{49}$$

$$T_3 = (ks - M\lambda)\left(F'(\gamma^{n+1}) - F'(\gamma)^{AB}\right) = O(\Delta t^2) \tag{50}$$

We incorporate the terms into Eq. (47) as

$$\frac{\gamma^{n+1} - \gamma^*}{\widehat{\Delta t}} = \nabla^2\left(M\lambda F'(\gamma^{n+1}) - M\lambda\nabla^2\gamma^{n+1} + T_1 + T_2 + T_3\right) + S_\gamma^{n+1}. \tag{51}$$

Observe that the inclusion of T_1 formally limits us to convergence order 1.5. We define C according to (26) as

$$C = \gamma^{n+1} + kF'(\gamma^{n+1}), \tag{52}$$

Plugging in the definitions of T_1, T_2, T_3, and C into Eq. (51), cancelling like terms, and rearranging, we get

$$\frac{\gamma^{n+1} - \gamma^*}{\widehat{\Delta t}} = \nabla^2\left(sC - s^2\widehat{\Delta t}\nabla^2 C + (M\lambda - ks)\,F'(\gamma)^{AB} + s\gamma^{n+1} - 2s\gamma^{AB} + ks^2\widehat{\Delta t}\nabla^2 F'(\gamma)^{AB}\right) + S_\gamma^{n+1} \tag{53}$$

Using Eq. (52) to eliminate γ^{n+1} in Eq. (53) and defining

$$A = C - s\widehat{\Delta t}\nabla^2 C - kF'(\gamma^{n+1}) - 2\gamma^{AB} + ks\widehat{\Delta t}\nabla^2 F'(\gamma)^{AB}, \tag{54}$$

Eq. (53) becomes

$$A - s\widehat{\Delta t}\nabla^2 A = \gamma^* - 2\gamma^{AB} + \widehat{\Delta t}M\lambda\nabla^2 F'(\gamma)^{AB} + \widehat{\Delta t}S_\gamma^{n+1}. \tag{55}$$

Recall $\gamma^{n+1} = g'(C)$ as described in Section 3.1.2. Substituting this into Eq. (52) and rearranging, we get $kF'(\gamma^{n+1}) = C - g'(C)$. Substituting this into Eq. (54) and combining the right hand side into B, we get a nonlinear equation satisfied by C:

$$B = A + 2\gamma^{AB} - ks\widehat{\Delta t}\nabla^2 F'(\gamma)^{AB} \qquad\qquad g'(C) - s\widehat{\Delta t}\nabla^2 C = B. \tag{56}$$

From these expressions, we have our four-stage scheme:

1. Compute γ^* by advection using Eq. (46).
2. Solve the Helmholtz equation for A given in Eq. (55).
3. Solve the nonlinear equation for C given in Eq. (56).
4. Update γ^{n+1} as $\gamma^{n+1} = g'(C)$.

3.1.4. Optimization-based formulation of the nonlinear solve

We solve the nonlinear equation (56) for C by reformulating it as a minimization of the objective function

$$E = \sum_i g(C_i) - \frac{1}{2} s\widehat{\Delta t} \sum_{i,j} C_i L_{ij} C_j - \sum_i C_i B_i, \tag{57}$$

where L is the discrete Laplacian matrix. The corresponding gradient is

$$\frac{\partial E}{\partial C_i} = g'(C_i) - s\widehat{\Delta t} \sum_j L_{ij} C_j - B_i \tag{58}$$

so that the optimality conditions $\frac{\partial E}{\partial C_i} = 0$ reduce to (56). Since we will be using a Newton-based solver, we will also need the Hessian

$$\frac{\partial^2 E}{\partial C_i \partial C_j} = \delta_{ij} g''(C_i) - s\widehat{\Delta t} L_{ij}. \tag{59}$$

Since $g''(C_i) > 0$, the Hessian is symmetric and positive definite. The optimization problem is thus convex, guaranteeing a unique local minimum, which is also the global minimum. We solve this optimization problem using Newton's method with Wolfe conditions line searches. We use zero as the initial guess during the first time step and C^{n-1} as the initial guess for the second time step. Thereafter, we warm-start our solver using $C^{AB} = 2C^{n-1} - C^{n-2}$ as the initial guess.

3.1.5. Boundary conditions

We consider two types of boundary conditions for γ: periodic and Neumann ($\mathbf{n} \cdot \nabla \gamma^{n+1} = 0$). In order to solve both implicit equations, we need boundary conditions for C and A. From $\gamma^{n+1} = g'(C)$ we have

$$\mathbf{n} \cdot \nabla \gamma^{n+1} = g''(C)\,(\mathbf{n} \cdot \nabla C)\,. \tag{60}$$

As $g''(C) \neq 0$, $\mathbf{n} \cdot \nabla \gamma^{n+1} = 0$ implies $\mathbf{n} \cdot \nabla C = 0$. For $\mathbf{n} \cdot \nabla A$, we start by substituting Eq. (52) into Eq. (54):

$$A = C - s\widehat{\Delta t}\nabla^2 \gamma^{n+1} - ks\widehat{\Delta t}\nabla^2 F'(\gamma^{n+1}) - 2\gamma^{AB} + ks\widehat{\Delta t}\nabla^2 F'(\gamma)^{AB} - kF'(\gamma^{n+1}) \tag{61}$$

$$= \gamma^{n+1} - 2\gamma^{AB} + s\widehat{\Delta t}\left(F'(\gamma^{n+1}) - \nabla^2 \gamma^{n+1}\right) - s\widehat{\Delta t}F'(\gamma^{n+1}) - ks\widehat{\Delta t}\nabla^2\left(F'(\gamma^{n+1}) - F'(\gamma)^{AB}\right). \tag{62}$$

As in [36], we define ξ^{n+1} to be a discrete version of the chemical potential following the derivation in Section 3.1.3 as

$$\xi^{n+1} = \lambda\left(F'(\gamma^{n+1}) - \nabla^2 \gamma^{n+1} + \frac{2s}{M\lambda}\left(\gamma^{n+1} - \gamma^{AB}\right) - k\nabla^2\left(F'(\gamma^{n+1}) - F'(\gamma)^{AB}\right) - \frac{(M\lambda - ks)}{M\lambda}\left(F'(\gamma^{n+1}) - F'(\gamma)^{AB}\right)\right). \tag{63}$$

Substituting in our equation for A leads to

$$A = \left(k - s\widehat{\Delta t}\right) F'(\gamma)^{AB} - \left(\gamma^{n+1} + kF'(\gamma^{n+1})\right) + \frac{s\widehat{\Delta t}}{\lambda}\xi^{n+1}. \tag{64}$$

Recognizing that $\mathbf{n} \cdot \nabla F'(\gamma) = F''(\gamma)\,(\mathbf{n} \cdot \nabla\gamma)$, the boundary condition for A is

$$\mathbf{n} \cdot \nabla A = \left(k - s\widehat{\Delta t}\right)\left(2F''(\gamma^n)\,(\mathbf{n} \cdot \nabla\gamma^n) - F''(\gamma^{n-1})\left(\mathbf{n} \cdot \nabla\gamma^{n-1}\right)\right) - \mathbf{n} \cdot \nabla\gamma^{n+1} - kF''(\gamma^{n+1})\left(\mathbf{n} \cdot \nabla\gamma^{n+1}\right) + \frac{s\widehat{\Delta t}}{\lambda}\mathbf{n} \cdot \nabla\xi^{n+1} \tag{65}$$

$$= \frac{s\widehat{\Delta t}}{\lambda}\mathbf{n} \cdot \nabla\xi^{n+1}, \tag{66}$$

where we have used $\mathbf{n} \cdot \nabla\gamma^{n-1} = \mathbf{n} \cdot \nabla\gamma^n = \mathbf{n} \cdot \nabla\gamma^{n+1} = 0$. Following [36] we use the boundary condition $\mathbf{n} \cdot \nabla\xi^{n+1} = 0$, which leads to $\mathbf{n} \cdot \nabla A = 0$. This gives us the necessary boundary conditions for both of our systems.

3.2. Navier-Stokes equations

3.2.1. Temporal discretization

We discretize the Navier-Stokes equations as in Goulding et al. [27]. As in Section 3.1.3, we discretize the time derivative as $\frac{\alpha\rho^{n+1}\mathbf{u}^{n+1} - \alpha(\rho\mathbf{u})^{BD}}{\Delta t}$. For the first time step, $\alpha = 1$ and $(\rho\mathbf{u})^{BD} = \rho^n\mathbf{u}^n$. To achieve second-order accuracy, we thereafter use a backwards-difference scheme with $\alpha = \frac{3}{2}$ and $(\rho\mathbf{u})^{BD} = \frac{4}{3}\rho^n\mathbf{u}^n - \frac{1}{3}\rho^{n-1}\mathbf{u}^{n-1}$. Explicit quantities for $\mathbf{u}$ are discretized using Adams-Bashforth, where $\mathbf{u}^{AB} = \mathbf{u}^n$ in the first time step and $\mathbf{u}^{AB} = 2\mathbf{u}^n - \mathbf{u}^{n-1}$ afterwards. As before, $\Delta t = \alpha\widehat{\Delta t}$ is used to simplify the equations. $\mathbf{u}^v$ is an intermediate estimate of $\mathbf{u}^{n+1}$ using an approximation for pressure, which is computed in an intermediate implicit solve, and $\mathbf{m}$ is the total density flux detailed in Section 3.2.2. With these, the discretized equations are

$$\frac{\rho^{n+1}\mathbf{u}^* - (\rho\mathbf{u})^{BD}}{\widehat{\Delta t}} + \nabla \cdot \left(\mathbf{m} \otimes \mathbf{u}^{AB}\right) = 0 \tag{67}$$

$$\frac{\mathbf{u}^{**} - \mathbf{u}^*}{\widehat{\Delta t}} = -\frac{1}{\rho^{n+1}}\nabla p^n + g + \frac{1}{\rho^{n+1}}\sigma\kappa\nabla\left(h\left(\gamma^{n+1}\right)\right) + \frac{1}{\rho^{n+1}}\nabla \cdot \left(\mu^{n+1}\left(\nabla\mathbf{u}^{AB}\right)^T\right) + \frac{1}{\rho^{n+1}}S_{\mathbf{u}}^{n+1} \tag{68}$$

$$\frac{\mathbf{u}^v - \mathbf{u}^{**}}{\widehat{\Delta t}} = \frac{1}{\rho^{n+1}}\nabla \cdot \left(\mu^{n+1}\nabla\mathbf{u}^v\right) \tag{69}$$

$$\nabla \cdot \left(\frac{1}{\rho^{n+1}}\nabla p'\right) = \frac{\nabla \cdot \mathbf{u}^v}{\widehat{\Delta t}} \tag{70}$$

$$\frac{\mathbf{u}^{n+1} - \mathbf{u}^v}{\widehat{\Delta t}} = -\frac{1}{\rho^{n+1}}\nabla p'. \tag{71}$$

3.2.2. Momentum flux

Everything in the Navier-Stokes equations is independent of Cahn-Hilliard except for the density flux term $\mathbf{m}$. We follow Huang et al. [36] and Goulding et al. [27] and give a modification of $\mathbf{m}$ here that is consistent with our new Cahn-Hilliard discretization in Section 3.1.3. Beginning with

$$\frac{\rho^{n+1} - \rho^{BD}}{\widehat{\Delta t}} + \nabla \cdot \mathbf{m} = S_m^{n+1}, \tag{72}$$

where $\mathbf{m}$ includes advection and Cahn-Hilliard separation, and S_m takes the effects of the forcing term S_γ, we express $\mathbf{m}$ in terms of γ:

$$\nabla \cdot \mathbf{m} = -\frac{\rho^{n+1} - \rho^{BD}}{\widehat{\Delta t}} + S_m^{n+1} \tag{73}$$

$$= -(\rho_1 - \rho_0)\frac{\gamma^{n+1} - \gamma^{BD}}{\widehat{\Delta t}} + S_m^{n+1} \tag{74}$$

$$= -(\rho_1 - \rho_0)\left(\frac{\gamma^{n+1} - \gamma^*}{\widehat{\Delta t}} + \frac{\gamma^* - \gamma^{BD}}{\widehat{\Delta t}}\right) + S_m^{n+1}. \tag{75}$$

Using Equations (46), (52), (54), and (55), defining $S_m^{n+1} = (\rho_1 - \rho_0) S_\gamma^{n+1}$, and canceling terms, this becomes

$$\nabla \cdot \mathbf{m} = (\rho_1 - \rho_0)\left(\nabla \cdot \left(\mathbf{u}^{AB}\gamma^{AB}\right) - \nabla \cdot \left(s\nabla C + s\nabla A + (M\lambda - as)\nabla F'(\gamma)^{AB}\right)\right). \tag{76}$$

As shown in [27], this definition of $\mathbf{m}$ is only well-defined up to a divergence-free shift. We determine the shift in the same way as in that work, by considering the case $\rho_0 = \rho_1$. This leads to the same shift of $\nabla \cdot \left(\rho_0 \mathbf{u}^{AB}\right)$ as in [27], which is consistent with the shift in [36]. We add this divergence-free shift to (76):

$$\nabla \cdot \mathbf{m} = \nabla \cdot \left(\rho_0 \mathbf{u}^{AB}\right) + (\rho_1 - \rho_0)\left(\nabla \cdot \left(\mathbf{u}^{AB}\gamma^{AB}\right) - \nabla \cdot \left(s\nabla C + s\nabla A + (M\lambda - as)\nabla F'(\gamma)^{AB}\right)\right). \tag{77}$$

This leads to a definition of

$$\mathbf{m} = \rho_0 \mathbf{u}^{AB} + (\rho_1 - \rho_0)\left(\mathbf{u}^{AB}\gamma^{AB} - s\nabla C - s\nabla A - (M\lambda - as)\nabla F'(\gamma)^{AB}\right). \tag{78}$$

Like in [27], the term $\mathbf{u}^{AB}\gamma^{AB}$ is replaced by the flux computed by the WENO conservative advection described in that work.

3.3. Discretization summary

For convenience, we provide a summary of a single step of the full discretized algorithm.

1. At the beginning of the step, the Adams-Bashforth and backwards-difference quantities must be computed from previous data. We compute γ^{BD} and γ^{AB} on cell centers and $(\rho\mathbf{u})^{BD}$ and $\mathbf{u}^{AB}$ on cell faces. First-order time discretizations are used on the first time step:

$$\gamma^{BD} = \gamma^n \qquad \gamma^{AB} = \gamma^n \qquad (\rho\mathbf{u})^{BD} = \rho^n\mathbf{u}^n \qquad \mathbf{u}^{AB} = \mathbf{u}^n \qquad \widehat{\Delta t} = \Delta t. \tag{79}$$

   Second-order time discretizations are used on every subsequence time step:

$$\gamma^{BD} = \frac{4}{3}\gamma^n - \frac{1}{3}\gamma^{n-1} \quad \gamma^{AB} = 2\gamma^n - \gamma^{n-1} \quad (\rho\mathbf{u})^{BD} = \frac{4}{3}\rho^n\mathbf{u}^n - \frac{1}{3}\rho^{n-1}\mathbf{u}^{n-1} \quad \mathbf{u}^{AB} = 2\mathbf{u}^n - \mathbf{u}^{n-1} \quad \widehat{\Delta t} = \frac{2}{3}\Delta t. \tag{80}$$

2. We use a conservative scheme as in [27] to compute γ^* from γ^{BD} as

$$\gamma^*_{i,j} = \gamma^{BD}_{i,j} - \widehat{\Delta t}\left(\frac{\mathcal{F}^W_{i+1/2,j} - \mathcal{F}^W_{i-1/2,j}}{\Delta x} + \frac{\mathcal{F}^W_{i,j+1/2} - \mathcal{F}^W_{i,j-1/2}}{\Delta y}\right), \tag{81}$$

   where the fluxes $\mathcal{F}^W$ are computed with WENO interpolation [39]. These fluxes are also stored for later use in computing the mass flux $\mathbf{m}$.

3. Next, we compute the intermediate term A from γ^* by solving the Helmholtz equation

$$A - s\widehat{\Delta t}\nabla^2 A = \gamma^* - 2\gamma^{AB} + \widehat{\Delta t} M\lambda\nabla^2 F'(\gamma)^{AB} + \widehat{\Delta t} S_\gamma^{n+1}. \tag{82}$$

4. We solve the nonlinear equation (56) for C by reformulating it as a minimization of the objective function

$$E = \sum_i g(C_i) - \frac{1}{2} s\widehat{\Delta t} \sum_{i,j} C_i L_{ij} C_j - \sum_i C_i B_i. \tag{83}$$

5. The final phase fraction γ^{n+1} is computed from C using g' (defined in (35)).

$$\gamma^{n+1} = g'(C), \tag{84}$$

6. With the Cahn Hilliard step complete, we begin the Navier-Stokes step. We compute effective densities and viscosities on faces by interpolating γ^{n+1} linearly to faces and then using equations (4) and (5).

$$\rho_{i+\frac{1}{2},j}^{n+1} = \rho_0 + (\rho_1 - \rho_0)\gamma_{i+\frac{1}{2},j}^{n+1} \tag{85}$$

$$\mu_{i+\frac{1}{2},j}^{n+1} = \mu_0 + (\mu_1 - \mu_0)\gamma_{i+\frac{1}{2},j}^{n+1}. \tag{86}$$

7. Compute the discrete mass flux using the Cahn-Hilliard intermediates A and C,

$$\mathbf{m} = \rho_0 \mathbf{u}^{AB} + (\rho_1 - \rho_0)\left(\mathcal{F}^W - s\nabla C - s\nabla A - (M\lambda - as)\nabla F'(\gamma)^{AB}\right). \tag{87}$$

8. Update momentum consistently with the movement of mass from Cahn-Hilliard as in [27]:

$$\rho^{n+1}\mathbf{u}^* = (\rho\mathbf{u})^{BD} - \widehat{\Delta t}\nabla\cdot\left(\mathbf{m}\otimes\mathbf{u}^{AB}\right). \tag{88}$$

9. Compute $\mathbf{u}^*$ by dividing off ρ^{n+1}.

10. Apply explicit forces:

$$\mathbf{u}^{**} = \mathbf{u}^* + \widehat{\Delta t}\mathbf{g} + \frac{\widehat{\Delta t}}{\rho^{n+1}}\sigma\kappa\nabla\left(h\left(\gamma^{n+1}\right)\right) + \frac{\widehat{\Delta t}}{\rho^{n+1}}\nabla\cdot\left(\mu^{n+1}\left(\nabla\mathbf{u}^{AB}\right)^T\right) - \frac{\widehat{\Delta t}}{\rho^{n+1}}\nabla p^n + \widehat{\Delta t} S_{\mathbf{u}}^{n+1} \tag{89}$$

Surface tension is descritized as in [27].

$$\kappa = -\nabla\cdot\left(\frac{\nabla\gamma}{||\nabla\gamma||}\right) \tag{90}$$

$$h(\gamma) = \begin{cases} 1, & \text{if } \gamma \geq 1-a \\ 0, & \text{if } \gamma < a \\ \frac{(-\gamma+a)^2(2\gamma+4a-3)}{(2a-1)^3}, & \text{otherwise} \end{cases} \tag{91}$$

$$a = 0.2 \tag{92}$$

The viscosity term is discretized consistently as in [36].

11. Solve the Helmholtz equation to apply the implicit portion of viscosity

$$\mathbf{u}^v - \frac{\widehat{\Delta t}}{\rho^{n+1}}\nabla\cdot\left(\mu^{n+1}\nabla\mathbf{u}^v\right) = \mathbf{u}^{**}. \tag{93}$$

12. Solve the Poisson equation for the pressure correction, and update the pressure:

$$\nabla \cdot \left(\frac{\widehat{\Delta t}}{\rho^{n+1}} \nabla p' \right) = \nabla \cdot \mathbf{u}^v \tag{94}$$

$$p^{n+1} = p^n + p', \tag{95}$$

13. Project $\mathbf{u}^{n+1}$ to be divergence free by applying the pressure correction:

$$\mathbf{u}^{n+1} = \mathbf{u}^v - \frac{\widehat{\Delta t}}{\rho^{n+1}} \nabla p'. \tag{96}$$

3.4. Note on convergence order

The formal convergence order for our method based on Taylor series expansion is 1.5, yet we observe second order in our numerical tests. The leading truncation errors in our method are of orders 1.5 and 2, so that our error can be approximated as $\epsilon = A\Delta t^{1.5} + B\Delta t^2$. Here, the coefficient A gets the T_1 term, which is the sole source of errors at this order. By contrast, nearly all of the discretization errors in the method are second order and belong in B, including all of the spatial discretization errors as well as the backward difference and Adams-Bashforth temporal discretizations.

In most schemes, the leading truncation terms are one order apart, such as $\epsilon = C\Delta t + D\Delta t^2 + O(\Delta t^3)$ or $\epsilon = C\Delta t^2 + D\Delta t^3 + O(\Delta t^4)$. If at some low resolution (say 10) the D term contributed an error one order larger than the coefficient C, then around this resolution a convergence order of about 1.91 would be observed. If the resolution is increased one order of magnitude to resolution 100, the two error terms would contribute equally, and a numerical convergence order 1.50 would be observed. If the resolution is increased by another order of magnitude to resolution 1000, the numerical convergence order would be measured at 1.09, by which point the leading error term would be apparent.

Next, consider the current scheme, where the leading errors are of the form $\epsilon = A\Delta t^{1.5} + B\Delta t^2$. Under the same conditions, where $B = 10A$ at resolution 10, a numerical convergence order of 1.95 is observed at this low resolution. By resolution 100, the order only drops to 1.88. By resolution 1000, the error is still only at 1.75. Only by resolution 16,000 does the observed convergence order drop as low as 1.6.

The actual situation is of course far more complex than this simple example. For example, if the A and B terms have different signs, then the convergence orders in the above example at resolutions 10, 100, 1000, and 16000 are instead 2.05, 2.23, undefined, and 1.33. Given this analysis, it is not entirely surprising that second order convergence would be observed numerically for the proposed scheme.

4. Numerical examples

We demonstrate the numerical properties of our scheme through a series of numerical tests. All the units in the following tests are SI units.

Table 1: At larger N, our Cahn-Hilliard scheme shows second order convergence at $t = 1$.

	$r = 0.1$				$r = 0.05$				$r = 0.01$			
N	L_2		L_∞		L_2		L_∞		L_2		L_∞	
8	1.28e-05		2.12e-05		1.28e-05		2.09e-05		1.27e-05		2.07e-05	
16	6.25e-06	1.04	1.27e-05	0.74	6.31e-06	1.02	1.27e-05	0.72	6.30e-06	1.01	1.27e-05	0.70
32	3.84e-06	0.70	1.22e-05	0.05	3.85e-06	0.71	1.22e-05	0.05	3.85e-06	0.71	1.23e-05	0.05
64	2.49e-06	0.63	1.14e-05	0.10	2.49e-06	0.62	1.15e-05	0.10	2.50e-06	0.62	1.15e-05	0.09
128	8.64e-07	1.52	4.85e-06	1.23	8.71e-07	1.52	4.90e-06	1.23	8.76e-07	1.51	4.94e-06	1.22
256	1.85e-07	2.22	1.05e-06	2.21	1.86e-07	2.22	1.05e-06	2.22	1.87e-07	2.22	1.06e-06	2.22
512	4.45e-08	2.05	2.55e-07	2.04	4.48e-08	2.06	2.57e-07	2.04	4.51e-08	2.06	2.59e-07	2.04

4.1. Manufactured solution

We test our discrete solvers using a manufactured solution for γ, $\mathbf{u}$, and p. Accuracy is measured by comparing the final simulated state against the manufactured solution. The source terms that enforce the manufactured solution are

$$S_\gamma = \frac{\partial \gamma}{\partial t} + \nabla \cdot (\mathbf{u}\gamma) - \nabla \cdot (M \nabla \xi) \tag{97}$$

$$S_{\mathbf{u}} = \frac{\partial \rho \mathbf{u}}{\partial t} + \nabla \cdot (\mathbf{m} \otimes \mathbf{u}) + \nabla p - \rho g - \sigma \kappa \nabla (h(\gamma)) - \nabla \cdot \left(\mu \left(\nabla \mathbf{u} + (\nabla \mathbf{u})^T \right) \right). \tag{98}$$

The accuracy of the Cahn-Hilliard solver is tested alone, then the Navier-Stokes solver is added for a second test of the full system. We also perform two additional tests to show that changes in r and b do not affect the accuracy of our solver. The parameters used follow the similar tests in [36] and [27]. All tests use a $[-\pi, \pi]^2$ domain and end at $t = 1$, with time step of $\Delta t = 0.08/N$ and cell size $\Delta x = 2\pi/N$. Fluid phase density is set to be $\rho_0 = 1$ and $\rho_1 = 3$ with viscosity constants $\mu_0 = 0.01$ and $\mu_1 = 0.02$. Unless otherwise noted, the Cahn-Hilliard parameters used in these tests are $M = 0.001$, $\lambda = 0.001$, $\eta = 0.1$, $r = 0.1$, and $b = 0.01$.

4.1.1. Cahn-Hilliard solver

To assess the convergence of the Cahn-Hilliard solver alone, we use the solution

$$\gamma(x, y, t) = \frac{1}{2} + \frac{10}{21} \cos(x) \cos(y) (1 - \sin(t)). \tag{99}$$

This solution is chosen such that $\mathbf{n} \cdot \nabla \gamma = 0$ and $\gamma \in (0, 1)$ within the time tested. We omit the Navier-Stokes update for this test and set $u = v = 0$. The initial conditions are set using the manufactured solution for $t = 0$. We refine N from 8 to 512 and use the L_2 and L_∞ errors at each level of refinement to measure the convergence rate. Table 1 shows that our Cahn-Hilliard solver exhibits second order convergence.

4.1.2. Cahn-Hilliard-Navier-Stokes solver

In this test, we repeat the test in Section 4.1.1 with the same solution for γ but this time with the coupled Cahn-Hilliard-Navier-Stokes solver and non-zero solutions for u, v, and p:

$$u(x, y, t) = \sin(x) \cos(y) \cos(t) \tag{100}$$

$$v(x, y, t) = -\cos(x) \sin(y) \cos(t) \tag{101}$$

$$p(x, y, t) = \cos(x) \cos(y) \sin(t), \tag{102}$$

Table 2: The coupled Cahn-Hilliard-Navier-Stokes scheme shows second order convergence at $t = 1$.

	γ				u				v				p			
N	L_2		L_∞		L_2		L_∞		L_2		L_∞		L_2		L_∞	
8	1.77e-02		3.39e-02		5.52e-02		1.35e-01		1.74e-02		4.50e-02		2.03e-02		4.64e-02	
16	2.98e-03	2.57	9.28e-03	1.87	1.23e-02	2.17	3.18e-02	2.08	3.43e-03	2.34	8.74e-03	2.36	4.01e-03	2.34	1.32e-02	1.82
32	5.68e-04	2.39	1.42e-03	2.71	3.04e-03	2.02	8.43e-03	1.92	7.64e-04	2.17	2.55e-03	1.78	8.43e-04	2.25	2.48e-03	2.41
64	1.39e-04	2.03	3.41e-04	2.06	7.59e-04	2.00	2.14e-03	1.97	1.88e-04	2.02	6.24e-04	2.03	2.10e-04	2.01	6.40e-04	1.95
128	3.49e-05	2.00	8.89e-05	1.94	1.91e-04	1.99	5.34e-04	2.01	4.81e-05	1.97	1.61e-04	1.96	5.49e-05	1.93	1.60e-04	2.00
256	8.77e-06	1.99	2.31e-05	1.94	4.82e-05	1.98	1.31e-04	2.02	1.36e-05	1.83	4.40e-05	1.87	1.57e-05	1.80	4.68e-05	1.77

Table 3: L_2 and L_∞ errors in γ for varying values of q.

q	b	L_2	L_∞
9.90e-01	1.32e+01	3.62e-05	9.11e-05
9.00e-01	1.20e+01	3.60e-05	9.05e-05
8.00e-01	1.07e+01	3.57e-05	8.99e-05
7.00e-01	9.33e+00	3.54e-05	8.93e-05
6.00e-01	8.00e+00	3.52e-05	8.89e-05
5.00e-01	6.67e+00	3.51e-05	8.85e-05
4.00e-01	5.33e+00	3.49e-05	8.84e-05
3.00e-01	4.00e+00	3.49e-05	8.83e-05
2.00e-01	2.67e+00	3.48e-05	8.84e-05
1.00e-01	1.33e+00	3.48e-05	8.86e-05
1.00e-02	1.33e-01	3.49e-05	8.89e-05
1.00e-03	1.33e-02	3.49e-05	8.89e-05
1.00e-04	1.33e-03	3.49e-05	8.89e-05
1.00e-05	1.33e-04	3.49e-05	8.89e-05
1.00e-06	1.33e-05	3.49e-05	8.89e-05

which are the same solutions used in [36] and [27]. These solutions provide a divergence-free velocity field throughout the test. We set gravity to $g = \langle 1, -2 \rangle$. The manufactured solutions are used to set the initial and boundary conditions. As in Section 4.1.1, N is refined from 8 to 256. The L_2 and L_∞ error is measured for γ, $\mathbf{u}$, and p at each level of refinement and used to measure the convergence rate. Second order convergence is observed in all quantities as shown in Table 2.

4.1.3. Varying b

Our time integration scheme includes one free parameter b. The convergence rate of the scheme is independent of this parameter, though the parameter is bounded by the restriction $0 < q < 1$ as noted in Section 3.1.2. To evaluate the effects of the constant b on the accuracy of the coupled Cahn-Hilliard and Navier-Stokes solvers, we fix $N = 128$ and instead vary b (or equivalently, q). We use the same manufactured solutions as in the previous tests. Table 3 shows that the solver accuracy (represented by the L_2 and L_∞ error of γ) is insensitive to the choice of b. Although accuracy is not appreciably affected by b, we observe that the scheme is more stable when b is large. This is somewhat expected, since the strength of the barrier is proportional to b, as one observes in (25) and (26). Indeed, if $b = 0$, the barrier is lost, and (25) reduces to a linear Helmholtz equation. Unless otherwise indicated, we run with $b = 0.01$ in all of our numerical examples, except when this would result in $q > 0.5$; in this case, we compute b so that $q = 0.5$.

Table 4: Analysis of manufactured solution error dependence on values of r.

(a) L_2 and L_∞ error for γ_1 at varying r values.

r	L_2	L_∞
4.00e-01	3.48e-05	8.88e-05
3.00e-01	3.49e-05	8.89e-05
2.00e-01	3.49e-05	8.89e-05
1.00e-01	3.49e-05	8.89e-05
1.00e-02	3.49e-05	8.89e-05
1.00e-03	3.49e-05	8.89e-05
1.00e-04	3.49e-05	8.89e-05
1.00e-05	3.49e-05	8.89e-05
1.00e-06	3.49e-05	8.89e-05

(b) L_2 and L_∞ error for γ_2 at varying r values.

r	L_2	L_∞
4.00e-01	1.33e-05	3.54e-05
3.00e-01	1.57e-05	4.32e-05
2.00e-01	1.81e-05	5.18e-05
1.00e-01	2.05e-05	6.13e-05
1.00e-02	2.28e-05	7.08e-05
1.00e-03	2.30e-05	7.18e-05
1.00e-04	2.31e-05	7.19e-05
1.00e-05	2.31e-05	7.19e-05
1.00e-06	2.31e-05	7.19e-05

4.1.4. Varying r

Our formulation of the potential F includes an extra free parameter r, which is the minimum of the double-well potential. In this test, we evaluate the effects of r on the accuracy of our solver. We test the coupled Cahn-Hilliard Navier-Stokes solver with two different manufactured solutions for γ over a range of values for r. The first solution is the same as in the previous manufactured solution tests,

$$\gamma_1(x, y, t) = \frac{1}{2} + \frac{10}{21}\cos(x)\cos(y)(1 - \sin(t)). \tag{103}$$

This solution has $\gamma \in [\frac{1}{42}, 1 - \frac{1}{42}]$, which means that as r becomes very small the barrier portion of F outside the minima will never be used. To account for this, we repeat this test using the second manufactured solution

$$\gamma_2(x, y, t) = \frac{1}{2}(1 - r)\left(1 + \cos\left(\frac{x}{2} + \frac{\pi}{2}\right)\cos\left(\frac{y}{2} + \frac{\pi}{2}\right)\right) + \frac{r}{2}. \tag{104}$$

so that $\gamma \in [\frac{r}{2}, 1 - \frac{r}{2}]$ extends into the tails of F. The following solutions for $\mathbf{u}$ and p are used in both cases:

$$u(x, y, t) = \sin(x)\cos(y)\cos(t) \tag{105}$$

$$v(x, y, t) = -\cos(x)\sin(y)\cos(t) \tag{106}$$

$$p(x, y, t) = \cos(x)\cos(y)\sin(t). \tag{107}$$

We fix $N = 128$ and vary r, as shown in Table 4. We observe that varying r does not strongly affect the accuracy, especially when r is small. This is consistent with the observation that F converges pointwise in the limit $r \to 0$, as can be seen in Figure 3. The barrier portion of the F becomes extremely sharp in this limit. Unlike traditional barrier methods, the sharpness of the barrier only weakly affects the performance of the method; although $F(\gamma)$ has a sharp barrier in the limits $\gamma \to 0$ and $\gamma \to 1$, $F(g'(C))$ only grows gradually as C approaches infinity. We do sometimes observe numerical difficulties when r is extremely small (below 10^{-4}). Unless otherwise specified, we run all of our tests with $r = 0.01$.

4.2. Binary separation of phases

We demonstrate fluid phase separation over time using a random initial γ distribution. No forces are calculated during this simulation and there is no γ source term. This test uses the same parameters as [27] and [32]. The domain

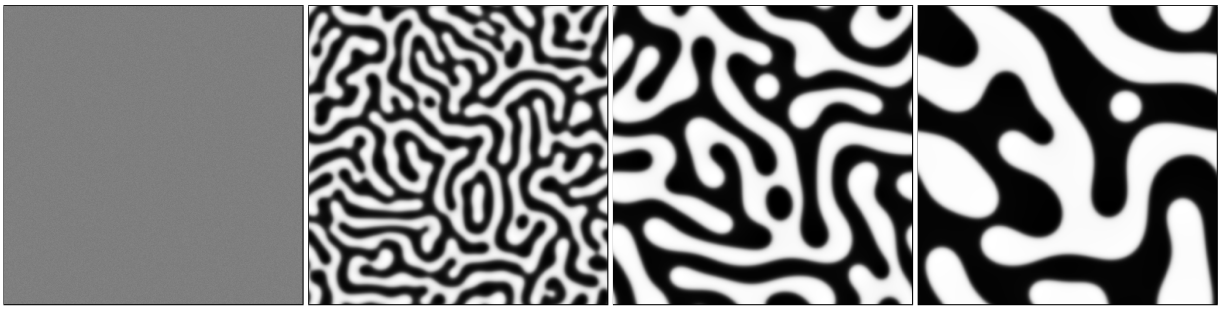

(a) $t = 0$ (b) $t = 0.1$ (c) $t = 1$ (d) $t = 5$

Fig. 6: Snapshots of phase separation over time.

is $[0, 2\pi]^2$ with periodic boundaries. The initial distribution is uniformly random in the range $[0.475, 0.575]$. The time step size is $\Delta t = 0.0001$ and the cell size is $\Delta x = 1/512$. The test runs until $t = 5$. The Cahn-Hilliard parameters are chosen to satisfy $ML = \eta^2 = 0.001$ with $\sigma = 1$. Figure 6 depicts the test results in several snapshots from $t = 0$ to $t = 5$. These snapshots are qualitatively similar to the results shown in [32], with increasing phase separation over time.

4.3. Stationary circle

We test the balance between pressure and surface tension forces by simulating a stationary circle of fluid. We take the test parameters from [36] and [27]. We measure the final velocity of the simulation to determine the magnitude of the spurious currents caused by force imbalance. We test 5 cases with differing density ratios, surface tension, and viscosity, and show how each case changes under refinement.

We use a $[0, 1]^2$ domain with free-slip boundary conditions and cell size $\Delta x = 1/N$. The test runs until $t = 10$ in time steps of $\Delta t = 0.064/N$. For each case we refine from $N = 16$ to $N = 256$. The circle of fluid is initialized at $(0.5, 0.5)$ with radius $r = 0.2$ and density $\rho_1 = 1000$. The viscosity of the circle differs depending on test case. The surrounding fluid varies in density and viscosity for each test case, and both fluids begin with no initial velocity. Table 5 lists the density, viscosity, and surface tension parameters for each case.

Following [36] and [27], we narrow the interface width η with refinement to show convergence to a sharp interface solution:

$$\eta = \eta_0 \left(\frac{\Delta x}{h_0} \right)^{X^\eta} = \eta_0 (N h_0)^{-X^\eta} \tag{108}$$

$$M = M_0 \left(\frac{\eta}{\eta_0} \right)^{X^M} = \frac{M_0}{N h_0} \tag{109}$$

$$\eta_0 = h_0 = \frac{1}{32} \qquad M_0 = 10^{-5} \qquad X^\eta = \frac{2}{3} \qquad X^M = \frac{3}{2}. \tag{110}$$

As in [36] and [27], we average the final velocity to cell centers and compare the magnitude $\|\mathbf{u}\|_2$ with the ideal value of 0. We compute the L_2 and L_∞ error and plot the change under refinement compared to the ideal first and second order case in Figure 7. Figure 7b shows that L_2 decreases with first order whenever viscosity is nonzero, though no

Table 5: Material parameters for the five tested stationary circle cases.

Case ID	ρ_0	ρ_1	μ_0	μ_1	σ
Case 1	1000	1000	0	0	1
Case 2	1000	1000	0.1	0.1	1
Case 3	1	1000	0.1	0.1	1
Case 4	1000	1000	0.0001	0.1	1
Case 5	1000	1000	0.1	0.1	10

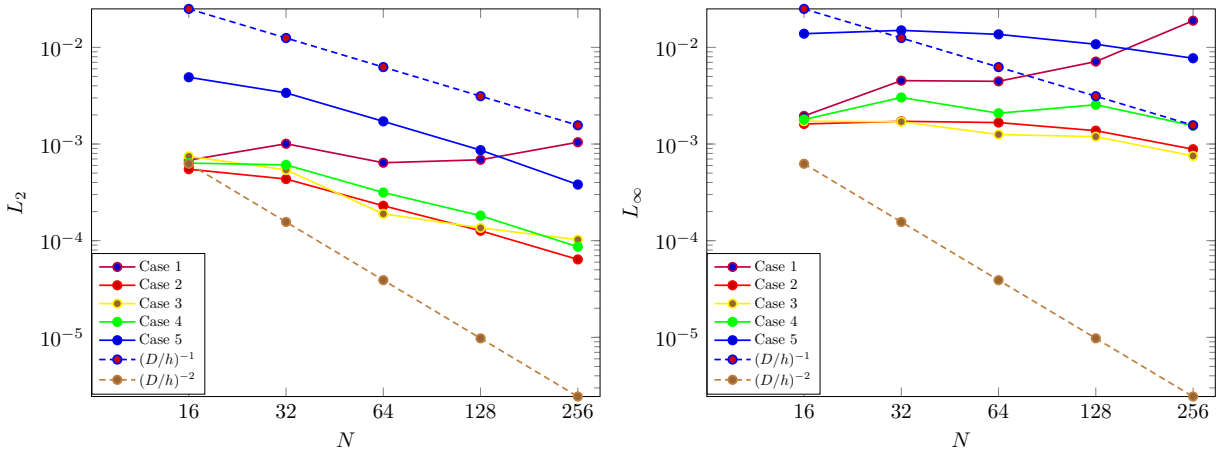

(a) L_2 error

(b) L_∞ error

Fig. 7: The magnitude of the spurious velocity for the five stationary circle cases at different resolutions.

improvement is observed in L_∞. That is, the maximum magnitude of velocity error does not change much, but the region over which this error occurs shrinks.

We note that the test above is not a proper convergence test, since the coefficients of the PDE are changing under refinement. As such, it is difficult to determine whether the problems observed are a consequence of the sharpening interface or a fundamental problem with the underlying scheme. To determine whether the proposed method is converging properly on this test, we hold the PDE fixed and perform a proper refinement study. We fix $\eta = 0.02$ and $M = 10^{-6}$. The results are shown in Figure 8, where we observe second order convergence in L_2 and convergence ranging from first to second order in L_∞.

From these tests, we conclude that the method converges but is somewhat sensitive to the sharpness of the interface. We suspect that this is related to the smoothness of the Cahn-Hilliard potential. The potential function F is C^3 continuous everywhere except at $\gamma = \frac{1}{2}$, where it is only C^2 continuous. This suffices to produce a continuous Hessian. However, the time integration scheme includes terms of the general form $\nabla^2 F'(\gamma)$, which when expanded out depend on the third derivative of F. This may introduce small discontinuities in the numerical scheme near the interface, which surface tension is particularly sensitive to.

4.4. Horizontal shear

We examine conservation of mass, conservation of momentum, and change in kinetic energy in a shearing advection test. Four cases with different density ratios and viscosities show the effects of these parameters on the test

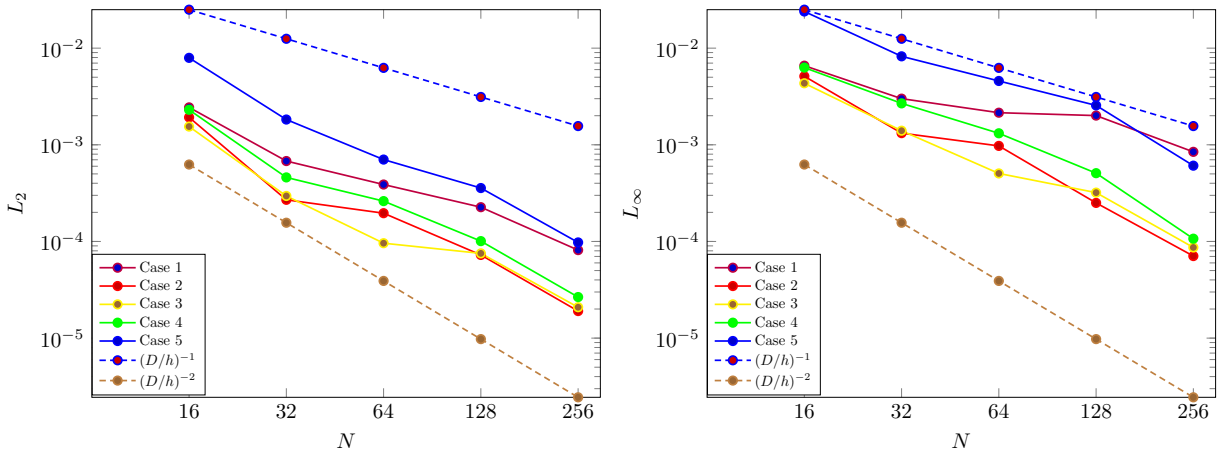

(a) L_2 error

(b) L_∞ error

Fig. 8: The magnitude of the spurious velocity for the five stationary circle cases with fixed interface width.

quantities. Surface tension and gravity are not used in this test.

The test setup is taken from [36] and [27]. The domain has periodic boundary conditions on all sides and has a range of $[0, 1]^2$. The time step size is $\Delta t = 0.0005$ and the tests run until $t = 1$. The cell size is $\Delta x = 1/128$. The surface tension constant is set to $\sigma = 10^{-12}$, leading to negligible surface tension forces, and $M = 10^{-7}$. The initial γ distribution is

$$\gamma(x, y, 0) = \begin{cases} \frac{1}{2}\left(1 + \tanh\left(\frac{y-y_1}{\delta_1}\right)\right), & \text{if } y \le y_0 \\ \frac{1}{2}\left(1 + \tanh\left(\frac{y_2-y}{\delta_1}\right)\right), & \text{if } y > y_0 \end{cases} \tag{111}$$

$$y_0 = 0.5 \qquad y_1 = 0.25 \qquad y_2 = 0.75 \qquad \delta_1 = 1/30, \tag{112}$$

with $\eta = \delta_1/\sqrt{2}$. The shearing velocity is

$$u(x, y, 0) = \begin{cases} \tanh\left(\frac{y-y_1}{\delta_1}\right), & \text{if } y \le y_0 \\ \tanh\left(\frac{y_2-y}{\delta_1}\right), & \text{if } y > y_0 \end{cases} \tag{113}$$

$$v(x, y, 0) = \delta_2 \sin(kx) \tag{114}$$

$$\delta_2 = 0.5 \qquad k = 2\pi. \tag{115}$$

These functions initialize fluid 1 with velocity in the postive x direction, located as a center band in the domain. Fluid 0 has a velocity in the negative x direction, and is located everywhere else. This distribution has a strong velocity gradient in the transition region between the fluids. Table 6 lists the variable parameters for the four different cases tested.

Following [27], we measured the change in total mass, total momentum, and kinetic energy using

$$m_{\text{total}} = \sum_{i,j} \left(\rho_0 + (\rho_1 - \rho_0)\,\gamma_{i,j}\right) \Delta x^2 \tag{116}$$

$$(m\mathbf{u})^x_{\text{total}} = \sum_{i,j} \left(\rho_{i-1/2,j}\right)\left(u_{i-1/2,j}\right) \Delta x^2 \tag{117}$$

$$E_k = \frac{1}{2} \sum_{i,j} \left(\left(\rho_{i-1/2,j}\right)\left(u_{i-1/2,j}\right)^2 + \left(\rho_{i,j-1/2}\right)\left(v_{i,j-1/2}\right)^2\right) \Delta x^2, \tag{118}$$

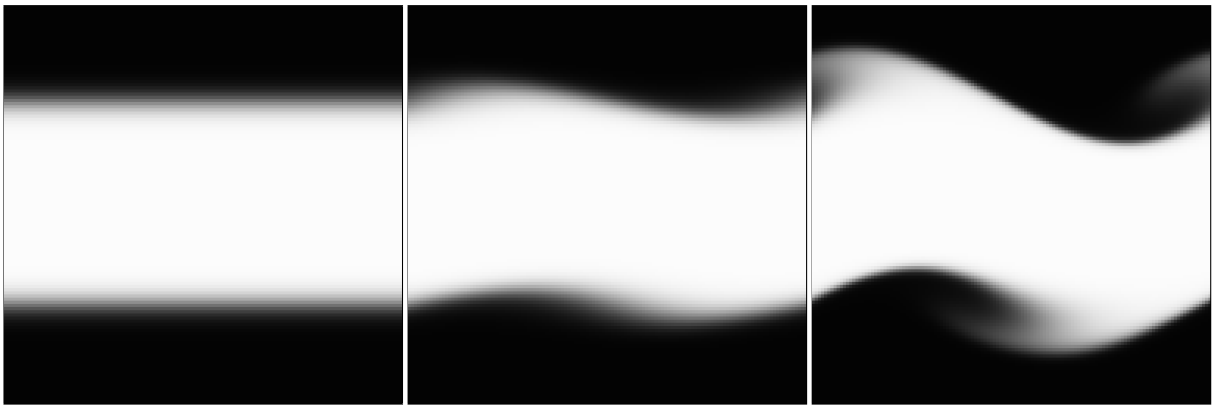

(a) $t = 0$ (b) $t = 0.5$ (c) $t = 1$

Fig. 9: Example of Horizontal Shear (Case 3).

with the y-axis momentum computed analogously to the x-axis. In the absence of surface tension and external forces, kinetic energy should only decrease in the viscous cases 3 and 4, and otherwise remain unchanged. In all four cases, momentum and mass should be conserved.

We plot the change in quantities ove time in Figure 10. In cases 1 and 3, where the fluids have matched densities, the density is constant throughout the domain and so mass is exactly conserved. In the other cases, there is a small change over time due to solver inaccuracies. Kinetic energy is conserved as expected in the inciscid cases 1 and 2, and declines due to viscosity in the remaining two cases. Momentum remains essentially unchanged in the y-axis, but we see a small negative trend over time in the x-axis. This change is on the order of our solver tolerances.

4.5. Translating circle

Based on the same test in [36] and [27], we test the accuracy of our coupled Cahn-Hilliard method with momentum advection. A drop of fluid 1 with radius 0.1 centered in the $[0, 1]^2$ domain is advected periodically with initial velocity $\langle 1, 1\rangle$ in the whole domain. We use cell size $\Delta x = 1/128$ and take time steps of $\Delta t = \Delta x/10$ until the simulation ends at time $t = 1$. The drop is expected to complete one full revolution and return to its initial position. The Cahn-Hilliard parameters are set as $M = 10^{-7}$ and $\eta = 3\Delta x$. We test with different densities for the fluid 1, ranging from $\rho_1 = 1$ to $\rho_1 = 10^9$. Fluid 0 has density $\rho_0 = 1$ in all cases. The resulting large density ratios demonstrate the robustness of our momentum conservation through advection. We do not test with viscosity or gravity. The tests are run twice, once with the surface tension constant $\sigma = 10^{-12}$, giving negligible surface tension force, and the the second time with $\sigma = 1$. The full set of cases are listed in Table 7.

Table 6: Material parameters for the four tested horizontal shear cases.

Case ID	ρ_0	ρ_1	μ_0	μ_1
Case 1	1	1	0	0
Case 2	1	10	0	0
Case 3	1	1	0.001	0.01
Case 4	1	10	0.001	0.01

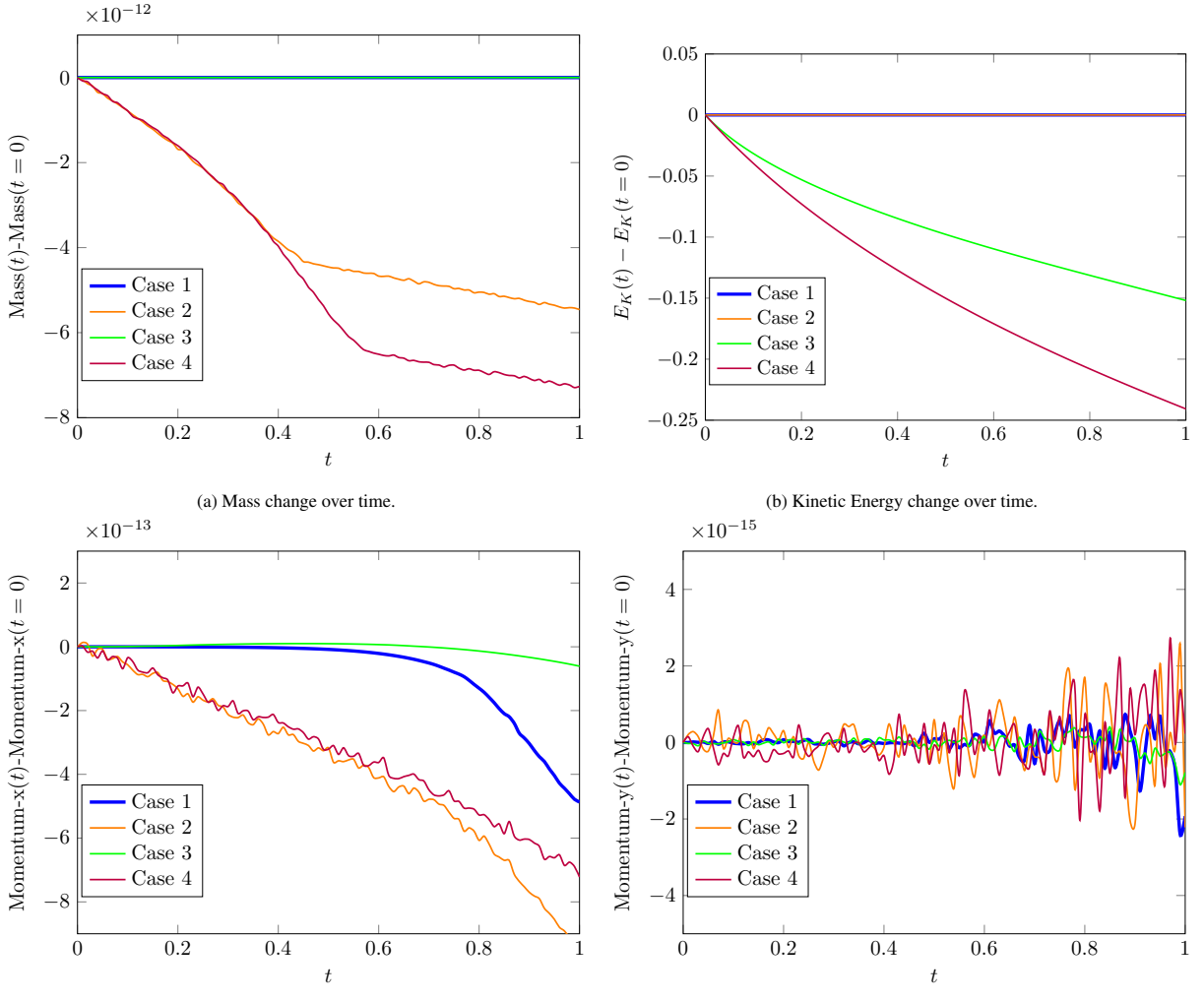

(a) Mass change over time.

(b) Kinetic Energy change over time.

(c) Momentum (x axis) change over time.

(d) Momentum (y axis) change over time.

Fig. 10: Conservation results for the four horizontal shear cases.

To evaluate the results of the test, we illustrate change in the velocity field as well as the shape of the drop. Ideally, the velocity field does not change from its initial $\langle 1, 1 \rangle$ values and the drop retains its circular shape. We measure the L_2 and L_∞ error in the velocity against its ideal values at the end of the simulation ($t = 1$). Figures 11 and Figure 12 depict the final state of the velocity field as staggered streamlines as well as the initial and final shape of the bubble. These figures may be compared to those produced by Huang et al. [36] in a similar test. We see that in all cases the numerical error is small enough that the velocity streamlines remain straight and the shape of the drop is preserved up to density ratios of $\rho_1/\rho_0 = 10^9$, overlapping visually with the exact solution.

Table 8 lists the measured error in the velocity field for the cases without surface tension. The velocity experiences negligible change at all density ratios. Table 9 lists the same measurements for the cases with surface tension. In this subset of cases, we see that there is more error in the velocity field, but this error decreases as the density ratio increases. In all cases, the measured error is at least as small as the results reported in [36] and [27].

Table 7: Material parameters for the eight translating circle cases.

Case ID	ρ_0	ρ_1	σ
Case 1	1	1	10^{-12}
Case 2	1	10^3	10^{-12}
Case 3	1	10^6	10^{-12}
Case 4	1	10^9	10^{-12}
Case 5	1	1	1
Case 6	1	10^3	1
Case 7	1	10^6	1
Case 8	1	10^9	1

Table 8: Velocity error for the four translating circle cases without surface tension (1–4).

Variable	Norm	$\rho_1/\rho_0 = 1$	$\rho_1/\rho_0 = 10^3$	$\rho_1/\rho_0 = 10^6$	$\rho_1/\rho_0 = 10^9$
u	L_2	8.73e-13	2.70e-13	2.92e-13	2.89e-13
	L_∞	7.33e-12	7.83e-13	8.76e-13	8.93e-13
v	L_2	8.73e-13	2.70e-13	2.92e-13	2.89e-13
	L_∞	7.33e-12	7.83e-13	8.76e-13	8.93e-13

Table 9: Velocity error for the four translating circle cases with surface tension (5–8).

Variable	Norm	$\rho_1/\rho_0 = 1$	$\rho_1/\rho_0 = 10^3$	$\rho_1/\rho_0 = 10^6$	$\rho_1/\rho_0 = 10^9$
u	L_2	7.87e-04	7.03e-06	7.35e-09	1.43e-10
	L_∞	6.36e-03	4.53e-05	4.77e-08	1.49e-09
v	L_2	7.87e-04	7.03e-06	7.35e-09	1.43e-10
	L_∞	6.36e-03	4.53e-05	4.77e-08	1.49e-09

4.6. Rising air bubble

We perform the rising air bubble test from [36] and [27] to examine how our scheme converges towards a sharp interface solution. We test 6 different ways of coupling the interface width parameter η to the resolution N and evaluate the results by measuring the circularity, center of mass, and rising velocity of a bubble surrounded by denser fluid.

We use a $[0, 1] \times [0, 2]$ domain with no-slip boundary conditions on the top and bottom edges and slip boundary conditions on the left and right edges. The cells are square with edge length $\Delta x = 1/N$. A circle of fluid 0 with diameter 0.5, density $\rho_0 = 1$, and viscosity $\mu_0 = 0.1$ begins centered at position $(0.5, 0.5)$. The surrounding fluid 1 has properties $\rho_1 = 1000$ and $\mu_1 = 10$. Gravity is set as $\langle 0, -0.98 \rangle$, and $\sigma = 1.96$. The fluid begins at rest, and the simulation runs until $t = 1$ with time step $\Delta t = 0.128/N$.

To couple η with N we use the following definitions from [36]:

$$\eta = \eta_0 (N h_0)^{-X_\eta} \tag{119}$$

$$M = M_0 (\eta/\eta_0)^{X_M}, \tag{120}$$

where $\eta_0 = h_0 = 1/32$ and $M_0 = 10^{-7}$. X_η and X_M are varied over the 6 different test cases, and we limit them with $X_\eta \leq 1$ based on [36] and $1 \leq X_M < 2$ from [38]. Each of the 6 test cases is refined from $N = 16$ to $N = 256$. For 5 of the tests we test the effects of varying X_η by fixing $X_M = 1$ and varying X_η in the range $[0, 1]$. In the final test, we

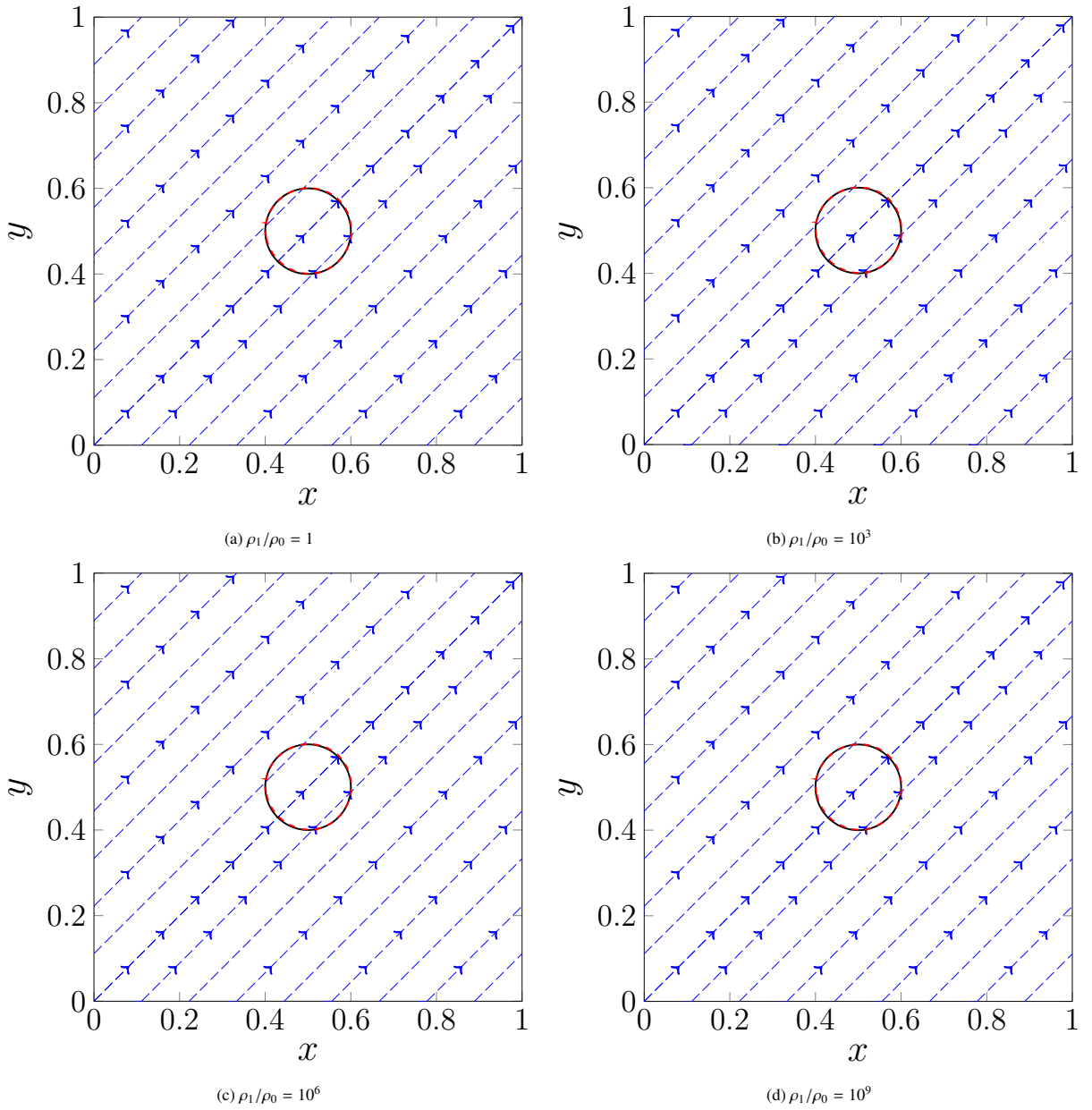

(a) $\rho_1/\rho_0 = 1$

(b) $\rho_1/\rho_0 = 10^3$

(c) $\rho_1/\rho_0 = 10^6$

(d) $\rho_1/\rho_0 = 10^9$

Fig. 11: The initial state of the translating circle (Cases 1–4) is represented by the solid black line. The final ($t = 1$) state is represented by the dashed red line. The blue dashed arrows represent the velocity streamlines at $t = 1$. We see that, as in the consistent momentum cases in [36], the streamlines appear straight and the drop shape is preserved up to a density ratio of 10^9.

increase X_M to $3/2$ and use $X_\eta = 2/3$, which keeps M proportional to Δx.

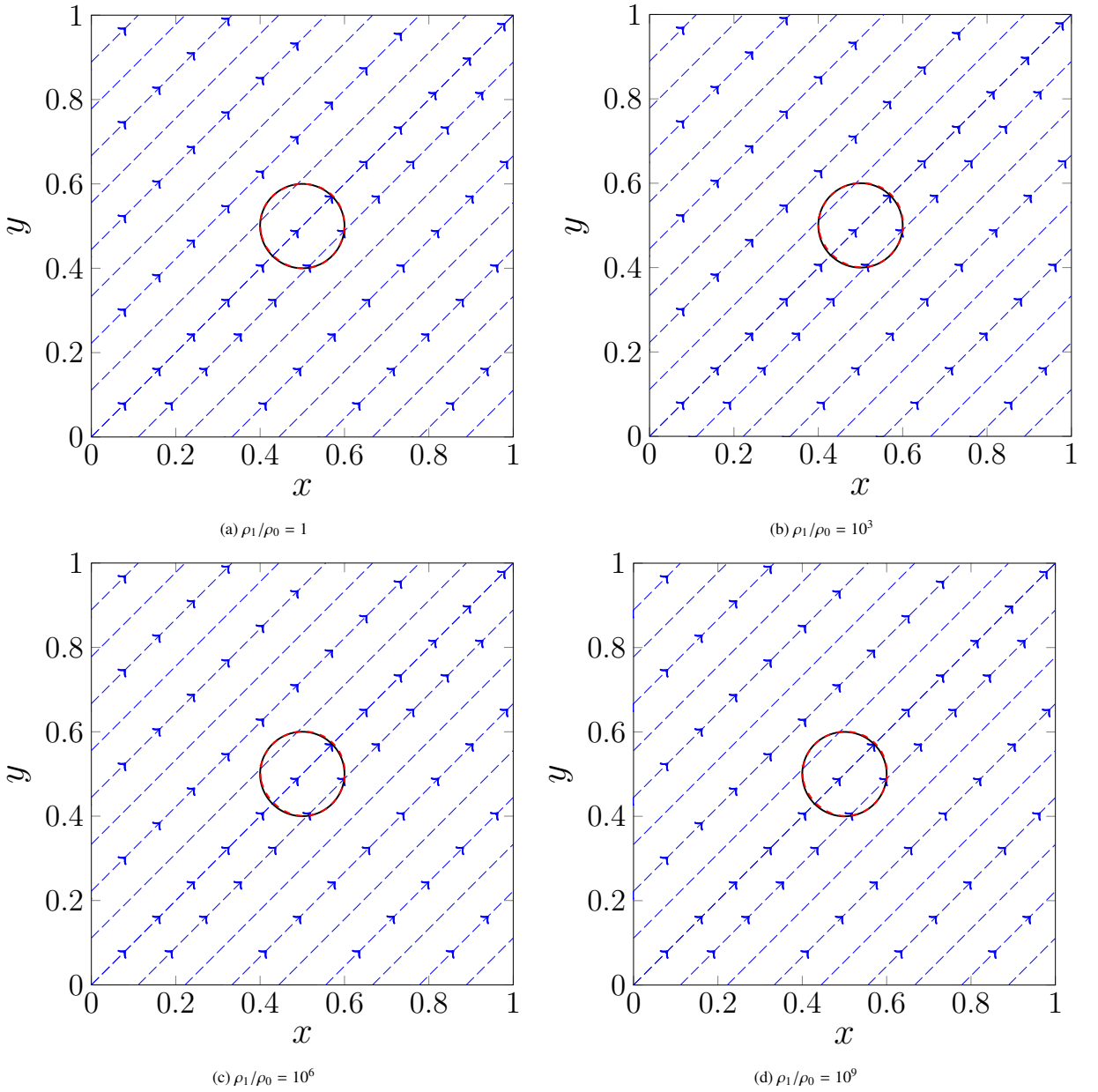

(a) $\rho_1/\rho_0 = 1$

(b) $\rho_1/\rho_0 = 10^3$

(c) $\rho_1/\rho_0 = 10^6$

(d) $\rho_1/\rho_0 = 10^9$

Fig. 12: The initial state of the translating circle (Cases 5–8) is represented by the solid black line. The final ($t = 1$) state is represented by the dashed red line. The blue dashed arrows represent the velocity streamlines at $t = 1$. We see that, as in the consistent momentum cases in [36], the streamlines appear straight and the drop shape is preserved up to a density ratio of 10^9.

To measure the circularity (ψ_c), center of mass (y_c), and rising velocity (v_c), we use the methods from [36]:

$$\psi_c = \frac{P_a}{P_b} = \frac{2\sqrt{\int_{\gamma<\frac{1}{2}} \pi d\Omega}}{P_b} \tag{121}$$

$$y_c = \frac{\int_\Omega y(1-\gamma)d\Omega}{\int_\Omega (1-\gamma)d\Omega} \tag{122}$$

$$v_c = \frac{\int_\Omega v(1-\gamma)d\Omega}{\int_\Omega (1-\gamma)d\Omega}, \tag{123}$$

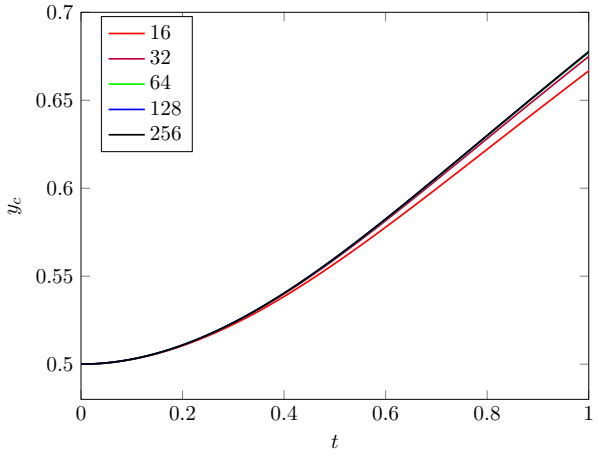

(a) Center of mass over time.

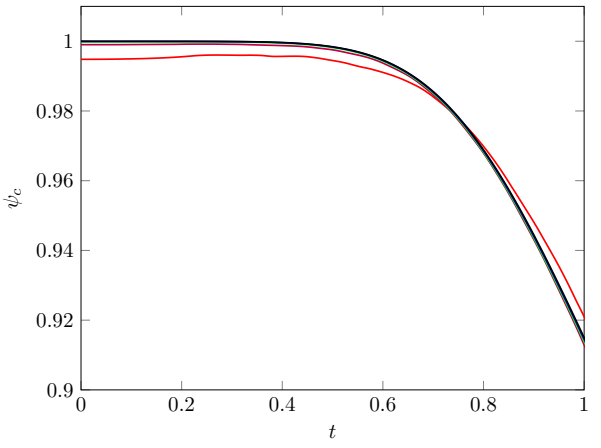

(b) Bubble circularity over time.

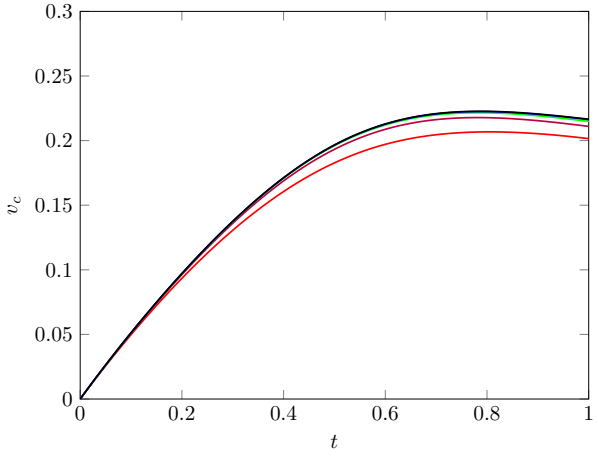

(c) Center of mass velocity over time.

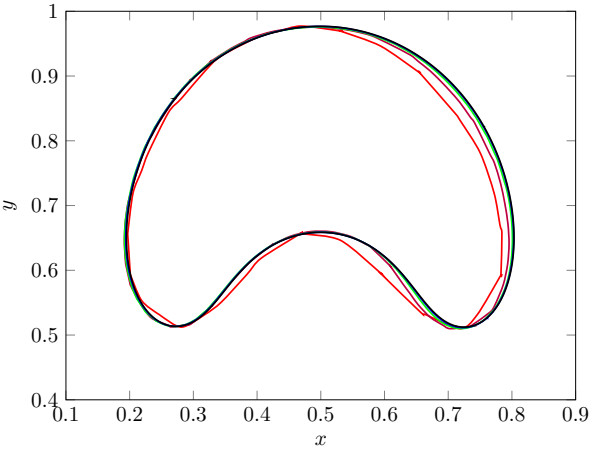

(d) Bubble surface at $t = 1$.

Fig. 13: Results for rising air bubble case 1.

with P_a is the perimeter of a reference circle the same area as the bubble and P_b is the perimeter of the bubble itself. Based on this ratio, when $\psi_c = 1$ the bubble is perfectly circular, and $\psi_c < 1$ will decrease as the bubble deforms. We compute P_b using the same method as [27].

We compare the measured values against the $N = 256$, using the L_2 error to measure the rate at which the test is converging to a solution. Table 10 details the error and convergence rate for each case. Our results are comparable to those reported in [36] and [27]. In case 1, the interface width should not change with refinement, so the simulated problem remains fixed at all N. We plot the change in our measured parameters over time for all refinements in Figure 13. We see in this figure that the parameters quickly converge to $N = 256$ values. Figure 14 demonstrates the differences between the 6 cases at the highest level of refinement with $N = 256$. Our results for this test match the results shown in [36] and [27].

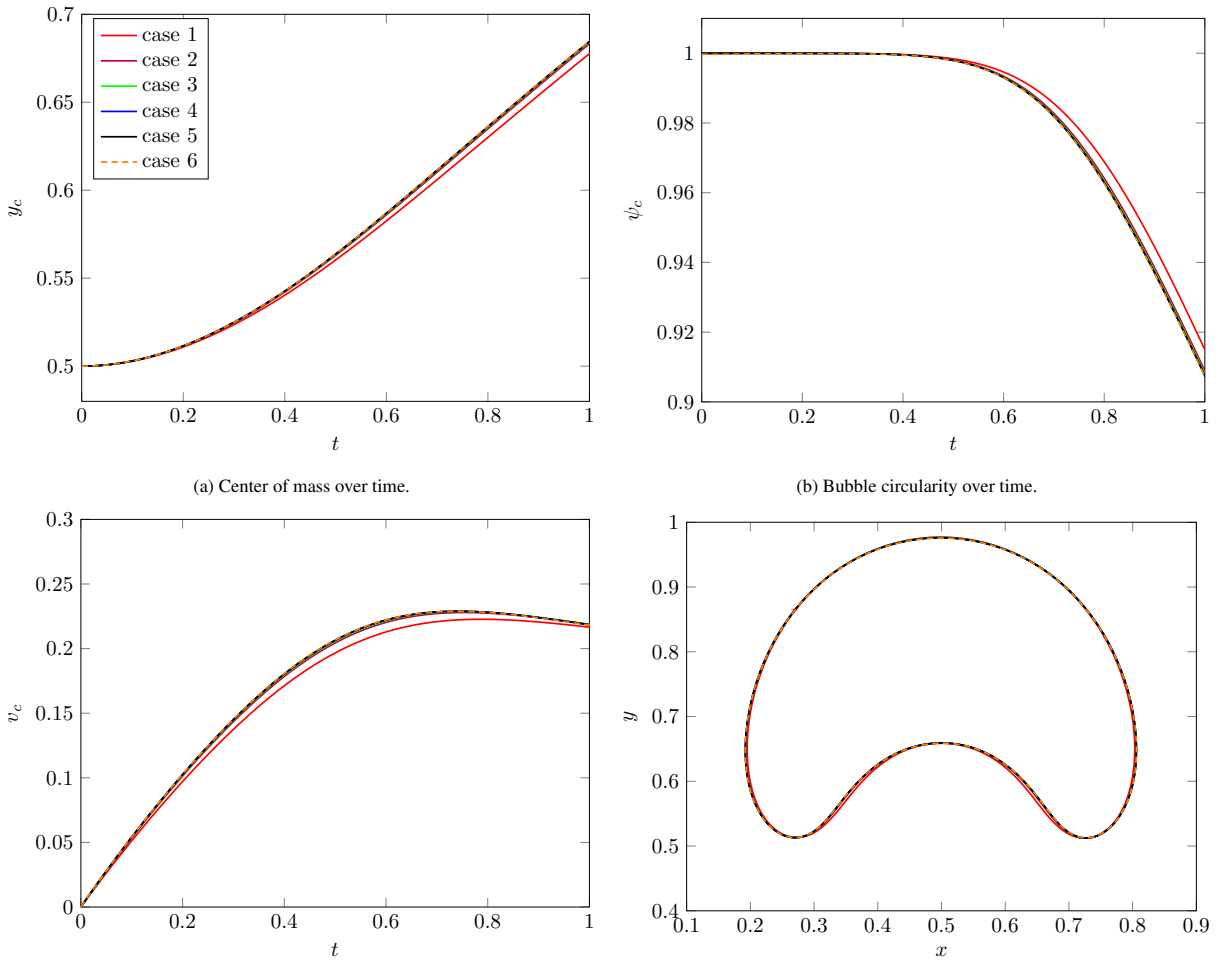

(a) Center of mass over time.

(b) Bubble circularity over time.

(c) Center of mass velocity over time.

(d) Bubble surface at $t = 1$.

Fig. 14: Comparing results for all rising bubble test cases with $N = 256$.

4.7. *Rayleigh-Taylor instability*

The Rayleigh-Taylor instability experiment from [49] is a classic multi-phase fluid simulation. As in [36] and [27], we reproduce this experiment with our scheme and measure key features over time.

The initial state positions a denser fluid with $\rho_1 = 3$ over a lighter fluid with $\rho_0 = 1$ in a $[0, 1] \times [0, 4]$ domain discretized with cell size $\Delta x = 1/128$. The domain is periodic in the x-axis and has free-slip boundary conditions at the top and bottom walls. The interface between the fluids is set to an unstable pertubation at $y = 2 + 0.1\cos(2\pi x)$, which will allow immediate mixing. The only external force applied is a gravity of $\langle 0, -1 \rangle$, and the fluids begin at rest. The characteristic parameter $A_t = (\rho_1 - \rho_0)/(\rho_1 + \rho_0)$, the "Atwood ratio", is used to scale the time step of $\Delta t = 5 \times 10^{-4}/\sqrt{A_t}$ and we run the simulation until $t\sqrt{A_t} = 8$. Both fluids have matched viscosity $\mu_0 = \mu_1 = 0.001$, and we set the surface tension constant $\sigma = 10^{-12}$ and the Cahn-Hilliard parameters as $\eta = 0.01$ and $\lambda M = 10^{-15}$

We show snapshots of this test in Figure 15 from $t\sqrt{A_t} = 0$ to $t\sqrt{A_t} = 2.5$ for our scheme and provide a comparison with our implementation of [27]. Figure 16 shows the continuation of the test using our scheme from $t\sqrt{A_t} = 2.25$

	Grid	$X_\eta = 0, X_M = 1$		$X_\eta = \frac{1}{3}, X_M = 1$		$X_\eta = \frac{1}{2}, X_M = 1$		$X_\eta = \frac{2}{3}, X_M = 1$		$X_\eta = \frac{2}{3}, X_M = \frac{3}{2}$		$X_\eta = 1, X_M = 1$	
		L_2		L_2		L_2		L_2		L_2		L_2	
ψ_c	16	4.91e-03		9.38e-03		1.14e-02		1.39e-02		1.38e-02		2.00e-02	
	32	1.61e-03	1.61	2.30e-03	2.03	2.78e-03	2.04	3.08e-03	2.17	3.06e-03	2.17	3.22e-03	2.64
	64	7.83e-04	1.04	8.71e-04	1.40	7.92e-04	2.04	7.22e-04	2.09	7.27e-04	2.08	8.61e-04	1.90
	128	3.02e-04	1.38	3.32e-04	1.39	2.83e-04	1.48	3.51e-04	1.04	3.66e-04	0.99	5.57e-04	0.63
		L_2		L_2		L_2		L_2		L_2		L_2	
y_c	16	7.80e-03		1.38e-02		1.58e-02		1.79e-02		1.79e-02		2.33e-02	
	32	2.01e-03	1.96	5.95e-03	1.21	6.60e-03	1.26	6.88e-03	1.38	6.87e-03	1.38	6.96e-03	1.74
	64	4.53e-04	2.15	2.60e-03	1.19	2.63e-03	1.26	2.43e-03	1.50	2.42e-03	1.50	1.88e-03	1.89
	128	9.74e-05	2.22	9.51e-04	1.45	8.64e-04	1.61	7.09e-04	1.78	7.01e-04	1.79	4.25e-04	2.14
		L_2		L_2		L_2		L_2		L_2		L_2	
v_c	16	1.34e-02		1.98e-02		2.20e-02		2.43e-02		2.43e-02		3.05e-02	
	32	4.48e-03	1.58	8.53e-03	1.21	9.19e-03	1.26	9.40e-03	1.37	9.38e-03	1.37	9.42e-03	1.69
	64	1.42e-03	1.66	3.64e-03	1.23	3.64e-03	1.26	3.34e-03	1.50	3.31e-03	1.50	2.65e-03	1.83
	128	3.00e-04	2.24	1.28e-03	1.50	1.20e-03	1.60	9.91e-04	1.75	9.70e-04	1.77	6.42e-04	2.04

Table 10: Rising air bubble test convergence results, using a comparison of simulations with $N = 16$ through $N = 128$ to corresponding simulations with $N = 256$.

to $t\sqrt{A_t} = 8$. Our results are visually comparable to the snapshots shown in [36] and [27], and maintain symmetry in the interface through the entire simulation. We also measure the location of the interface between the fluids from $t\sqrt{A_t} = 0$ to $t\sqrt{A_t} = 2.5$, plotting the highest and lowest point of the interface in Figure 18. Our results are similar to those of the experiments with similar parameters reported in [27], [36], [16] and [29]. As in these other works, the simulation does not reach a stable state in the time given.

As in [36] and [27], in Figure 17 we show a comparison of our scheme with different density values for fluid 1. We test densities $\rho_1 = 3, 30, 1000, 3000$, and our results for $t\sqrt{A_t} = 0$ to $t\sqrt{A_t} = 1.75$ are similar to those shown in previous works. However, we note that our interface does not maintain symmetry past $t\sqrt{A_t} = 4$ for the larger density ratios at the given parameters. [36] and [27] do not report past $t\sqrt{A_t} = 2$, so we cannot say whether this is a limitation of this approach or just our scheme.

4.8. Dam break

We simulate a dam break scenario as described in Martin and Moyce [46], where a rectangular volume of water at rest is released to flow in a larger container. This simulation shows how our scheme handles setups based on physical phenonmenon. The initial square of water with side length $a = 0.05715$ is positioned in the lower-left corner of the $[0, 4a] \times [0, 2a]$ domain. All walls in this domain are treated with the no-slip boundary condition, and each cell has size $\Delta x = a/64$. The initial velocity is zero everywhere in the domain. In our simulation, fluid 1 represents water with viscosity $\mu_1 = 1.002 \times 10^{-3}$ and density $\rho_1 = 998.207$. Fluid 2 represents air and has viscosity constant $\mu_0 = 1.78 \times 10^{-5}$ and density $\rho_0 = 1.204$. The surface tension constant is $\sigma = 7.28 \times 10^{-2}$ and gravity of $\langle 0, -9.8 \rangle$ is used as an external force. We set the Cahn-Hilliard parameters based on [36] and [27], which are $M\lambda = 10^{-7}$ and $\eta = 0.01a$. We take time steps of $\Delta t = 7.1437 \times 10^{-5}$ and run the simulation until $t = 10$.

As illustrated in Figures 20 and 21, when the simulation begins gravity causes the water to flow from the left edge to the right edge of the domain. The water's momentum causes it to rise up the right wall of the domain, where gravity overcomes the momentum and the water collapses back down on itself. Following [36] and [27], when reporting our

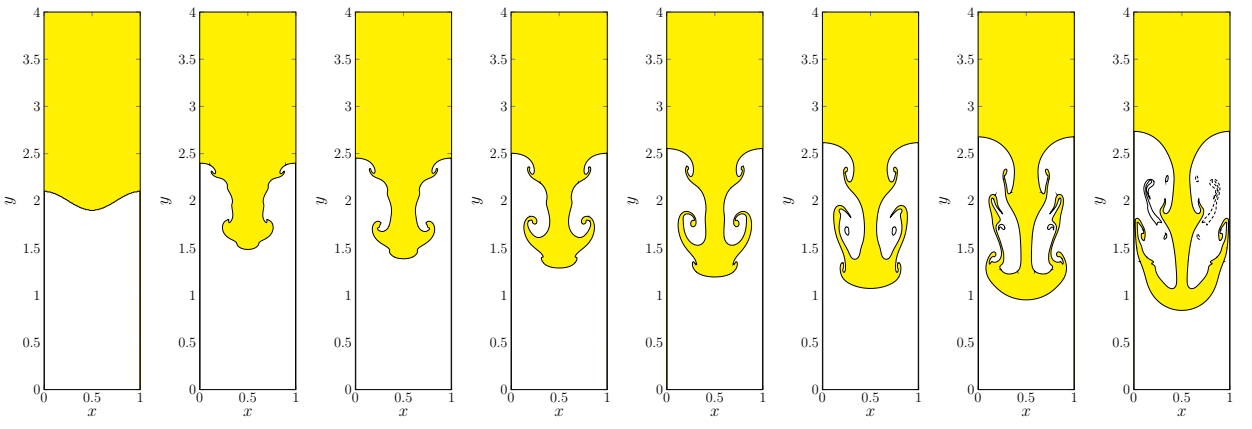

(a) Snapshots of a Rayleigh-Taylor simulation using Goulding et al. [27]'s method.

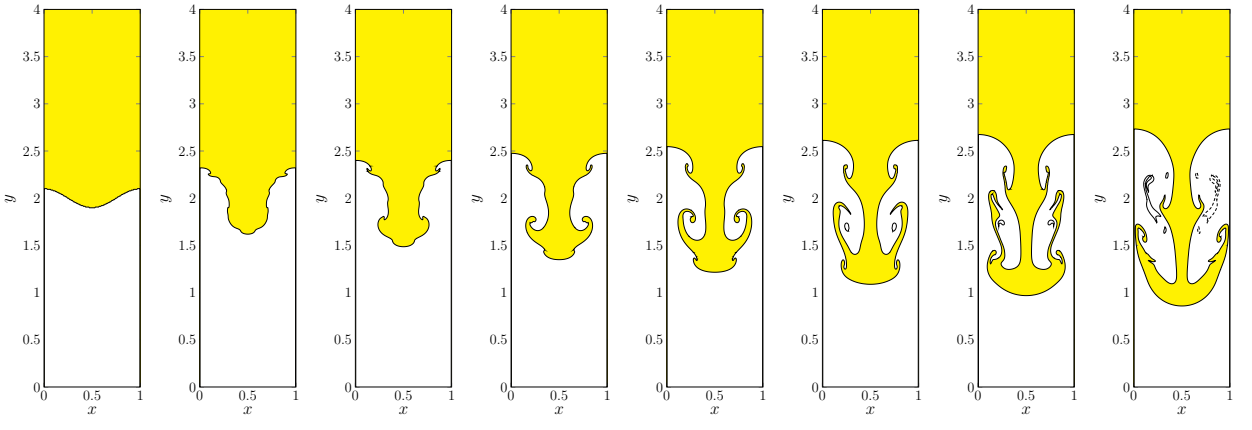

(b) Snapshots of a Rayleigh-Taylor simulation using our method.

Fig. 15: Visual comparison of Rayleigh-Taylor simulations using different methods at $t = 0, 1, 1.25, 1.5, 1.75, 2, 2.25, 2.5$.

results we non-dimensionalize t as $T = t\sqrt{\frac{|g_y|}{a}}$ and length by dividing by a. Figure 19 shows the location of the front of the water Z and the highest point H from $T = 0$ to $T = 2.25$. These results compare well to the canonical experiment results in Martin and Moyce [46] and the results reported in [36] and [27].

5. Conclusion

In this paper we constructed a novel discretization of the Cahn-Hilliard equations that is able to guarantee that phase fractions remain bounded between 0 and 1. Maintaining phase fractions in the feasible range is essential for stability, since values outside this range may produce negative densities, especially with large density ratios. The method eliminates the need to perform a global post-processing step to correct the phase fraction. We constructed a formally 1.5 order accurate time integration scheme that uses a barrier potential to maintain bounds on the phase fraction. We present a potential function that allows the barrier formulation to be cast as a convex nonlinear optimization problem, which can be solved efficiently and robustly. We coupled our Cahn-Hilliard solver to the Navier-Stokes equations to simulate phase separation in a two-phase fluid flow in two dimensions. The resulting solver is mass-momentum consistent and works with large density ratios. We demonstrate second order accuracy in γ and velocity and compare

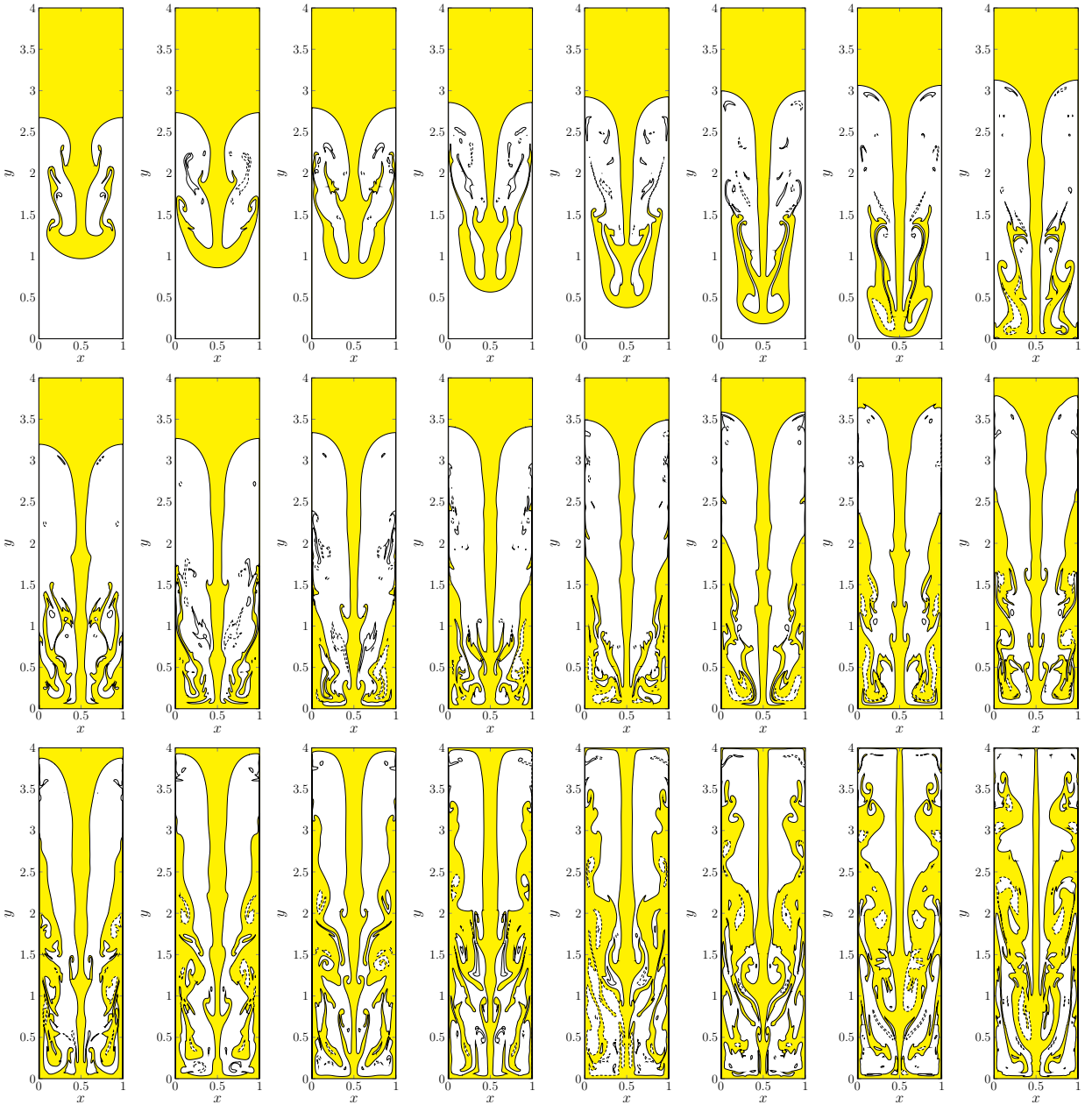

Fig. 16: Continued snapshots of a Rayleigh-Taylor simulation using our method with $\rho_0 = 3$, from $t = 2.25$ to $t = 8$ in 0.25 increments.

it with published results on a number of tests.

Since our method uses the same Navier-Stokes discretization and coupling as [27], we observe some of the same limitations, such as artifacts in the shearing test in Section 4.4. The method is sensitive to the sharpness of the interface, likely related to the lack of C^3 continuity in the potential F; unfortunately, the current formulation does not quite provide enough freedom to allow F to be C^3 everywhere. We have also observed that under some circumstances, the scheme suffers numerical difficulties or is not stable; this can occur when the parameters r or b are very small.

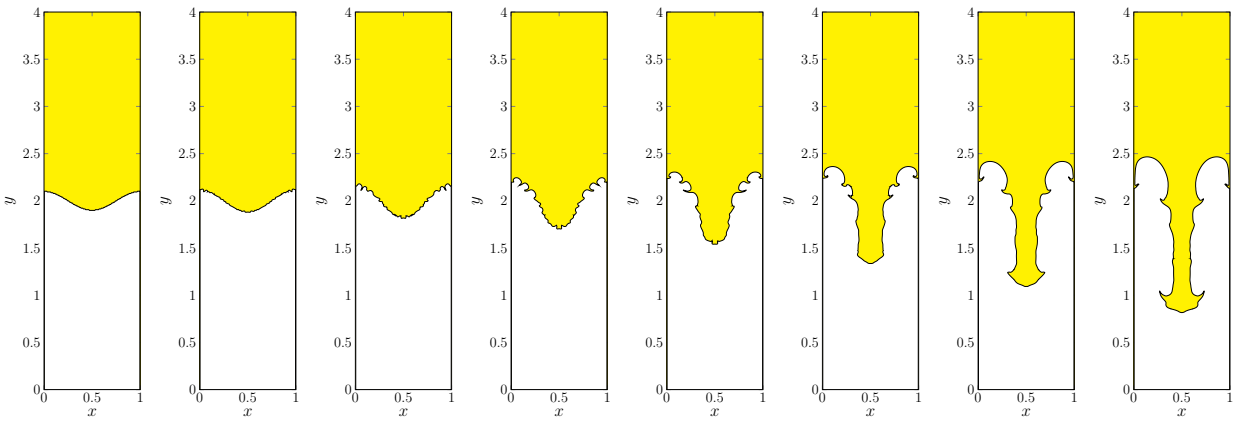

(a) $\rho_1 = 30$

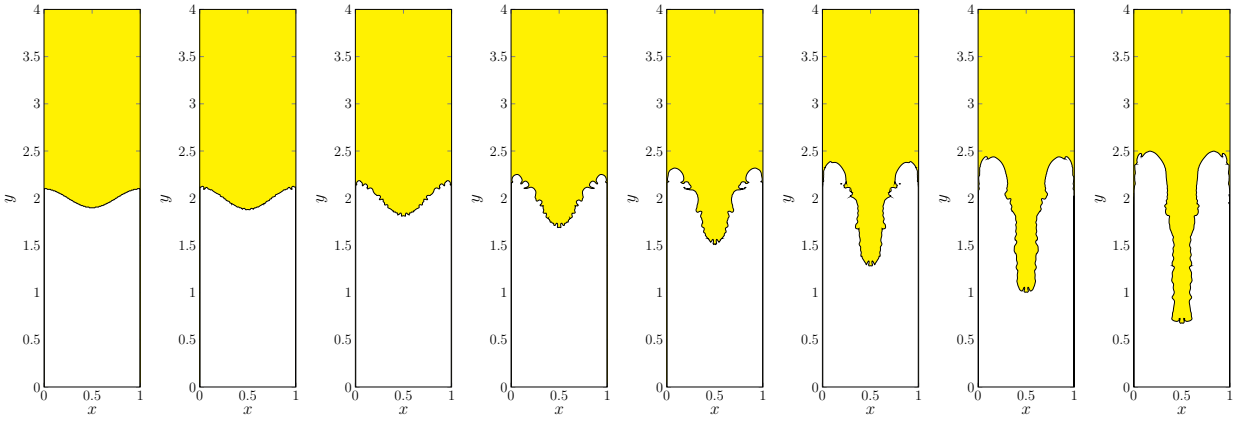

(b) $\rho_1 = 1000$

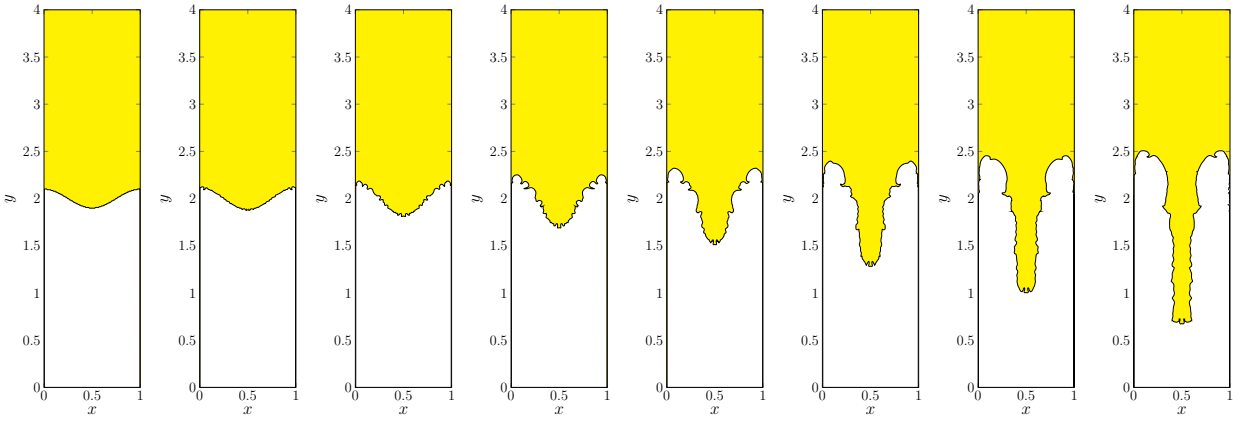

(c) $\rho_1 = 3000$

Fig. 17: Snapshots of Rayleigh-Taylor simulations with different density ratios at $t = 0, 0.25, 0.5, 0.75, 1, 1.25, 1.5, 1.75$.

6. Acknowledgements

This work was supported in part by National Science Foundation award NSF-2006570 as well as University of California award M23PL6076.

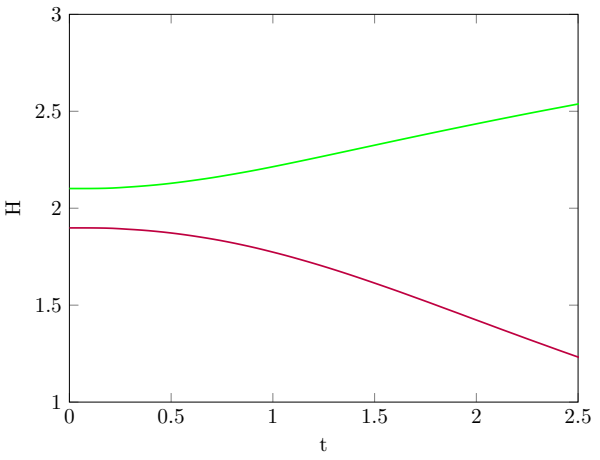

Fig. 18: Tracking the maximum and minimum y of the phase interface in the Rayleigh-Taylor simulation with $\rho_1/\rho_0 = 3$.

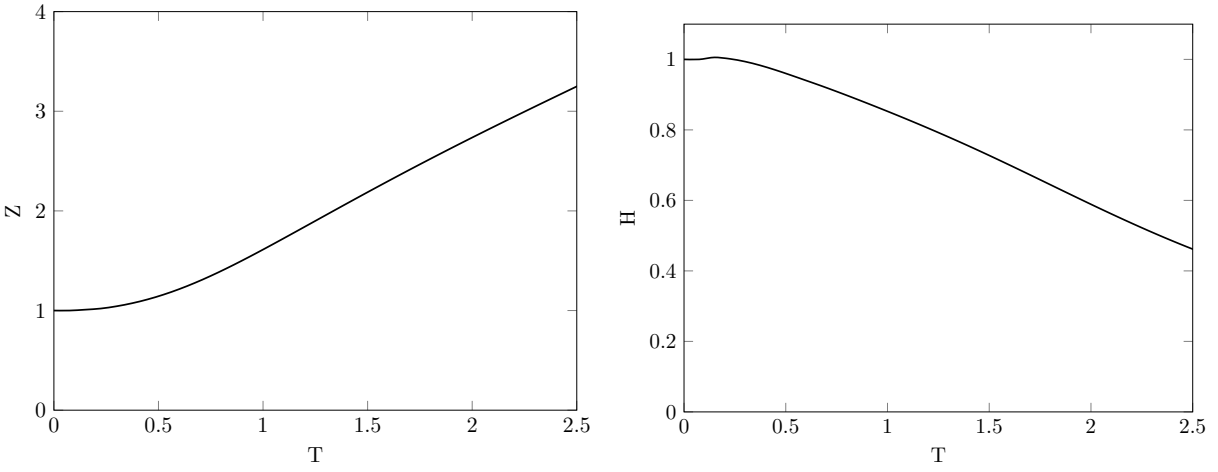

(a) The largest x location of fluid phase 1 over time.

(b) The largest y location of fluid phase 1 over time.

Fig. 19: Tracking the height and front of fluid phase 1 in the dam break scenario.

References

[1] Helmut Abels and Mathias Wilke. Convergence to equilibrium for the cahn–hilliard equation with a logarithmic free energy. *Nonlinear Analysis: Theory, Methods & Applications*, 67(11):3176–3193, 2007.

[2] Daniel Acosta-Soba, Francisco Guillén-González, and J Rafael Rodriguez-Galván. An upwind dg scheme preserving the maximum principle for the convective cahn-hilliard model. *Numerical Algorithms*, 92(3):1589–1619, 2023.

[3] VE Badalassi and S Banerjee. Nano-structure computation with coupled momentum phase ordering kinetics models. *Nuclear engineering and design*, 235(10-12):1107–1115, 2005.

[4] Vittorio E Badalassi, Hector D Ceniceros, and Sanjoy Banerjee. Computation of multiphase systems with phase field models. *Journal of computational physics*, 190(2):371–397, 2003.

[5] Rafael Bailo, José A Carrillo, Serafim Kalliadasis, and Sergio P Perez. Unconditional bound-preserving and energy-dissipating finite-volume schemes for the cahn-hilliard equation. *arXiv preprint arXiv:2105.05351*, 2021.

[6] John W Barrett and James F Blowey. An error bound for the finite element approximation of the cahn-hilliard equation with logarithmic free energy. *Numerische Mathematik*, 72:1–20, 1995.

[7] John W Barrett, James F Blowey, and Harald Garcke. Finite element approximation of the cahn–hilliard equation with degenerate mobility. *SIAM Journal on Numerical Analysis*, 37(1):286–318, 1999.

[8] James F Blowey and Charles M Elliott. The cahn–hilliard gradient theory for phase separation with non-smooth free energy part i: Mathematical analysis. *European Journal of Applied Mathematics*, 2(3):233–280, 1991.

[9] James F Blowey, MIM Copetti, and Charles M Elliott. Numerical analysis of a model for phase separation of a multicomponent alloy. *IMA Journal of Numerical Analysis*, 16(1):111–139, 1996.

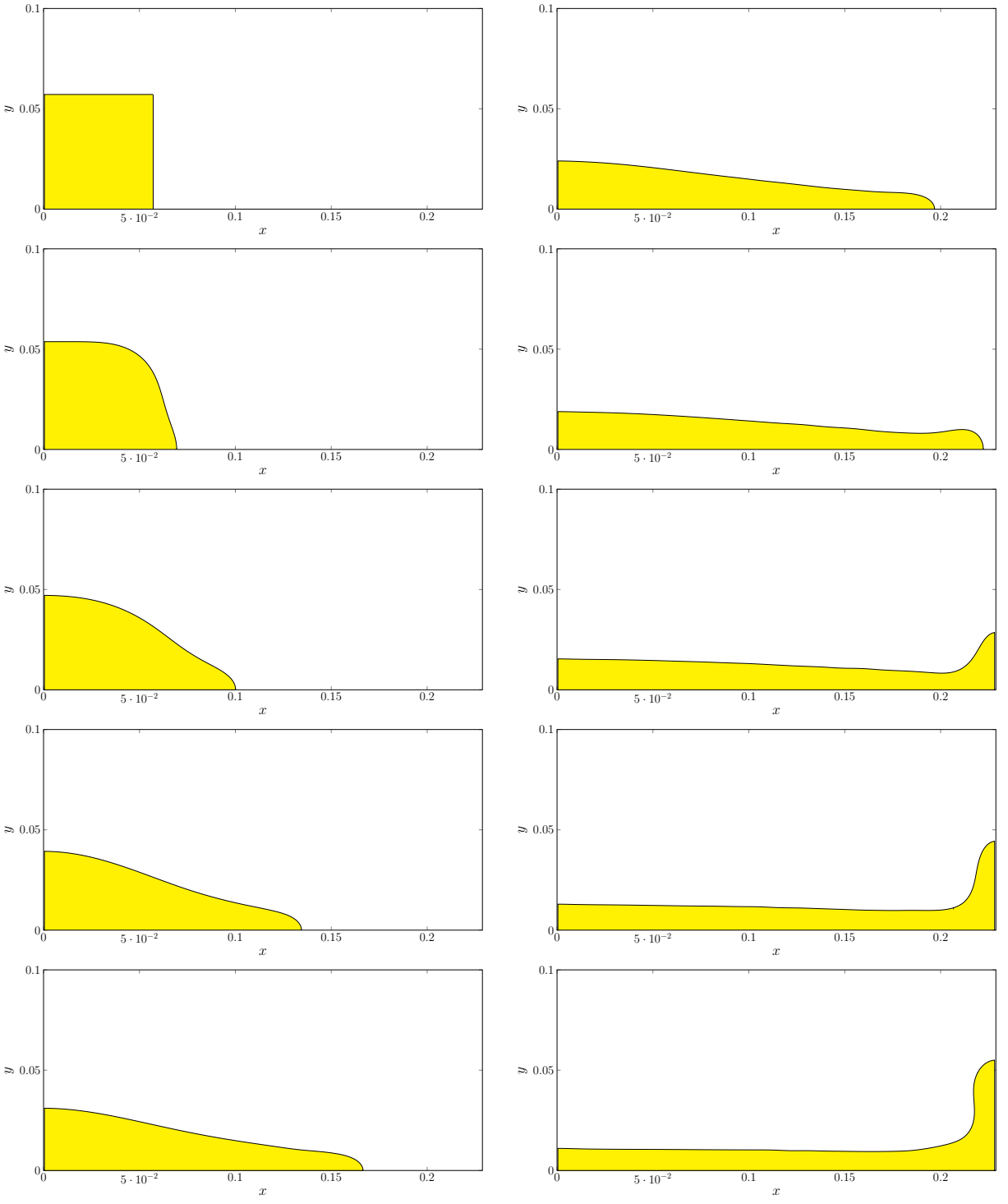

(a) $T = 0$ to $T = 2$

(b) $T = 2.5$ to $T = 4.5$

Fig. 20: Snapshots of the dam break scenario from $T = 0$ to $T = 4.5$.

[10] John W. Cahn and John E. Hilliard. Free energy of a nonuniform system. i. interfacial free energy. *The Journal of Chemical Physics*, 28(2): 258–267, 1958. doi: 10.1063/1.1744102. URL `https://doi.org/10.1063/1.1744102`.

[11] Wenbin Chen, Cheng Wang, Xiaoming Wang, and Steven M Wise. Positivity-preserving, energy stable numerical schemes for the cahn-hilliard equation with logarithmic potential. *Journal of Computational Physics: X*, 3:100031, 2019.

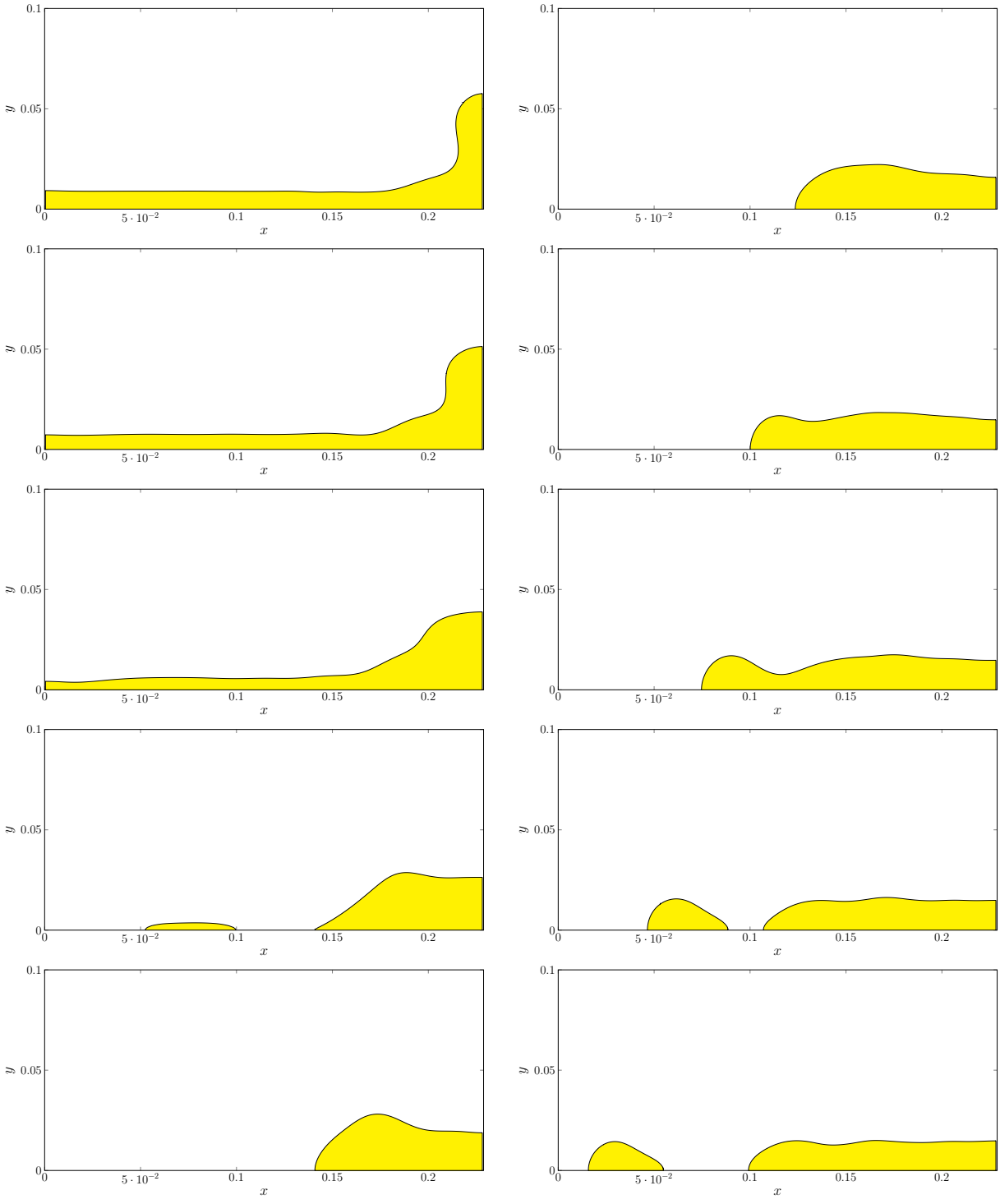

(a) $T = 5$ to $T = 7$

(b) $T = 7.5$ to $T = 9.5$

Fig. 21: Snapshots of the dam break scenario from $T = 5$ to $T = 9.5$.

[12] Kelong Cheng, Wenqiang Feng, Cheng Wang, and Steven M Wise. An energy stable fourth order finite difference scheme for the cahn–hilliard equation. *Journal of Computational and Applied Mathematics*, 362:574–595, 2019.

[13] Pao-Hsiung Chiu and Yan-Ting Lin. A conservative phase field method for solving incompressible two-phase flows. *Journal of Computational Physics*, 230(1):185–204, 2011.

[14] Maria Inês Martins Copetti and Charles M Elliott. Numerical analysis of the cahn-hilliard equation with a logarithmic free energy. *Numerische Mathematik*, 63:39–65, 1992.

[15] Arnaud Debussche and Lucia Dettori. On the cahn-hilliard equation with a logarithmic free energy. *Nonlinear Analysis: Theory, Methods & Applications*, 24(10):1491–1514, 1995.

[16] Hang Ding, Peter D.M. Spelt, and Chang Shu. Diffuse interface model for incompressible two-phase flows with large density ratios. *Journal of Computational Physics*, 226(2):2078–2095, 2007. ISSN 0021-9991. doi: https://doi.org/10.1016/j.jcp.2007.06.028. URL https://www.sciencedirect.com/science/article/pii/S0021999107002793.

[17] Lixiu Dong, Cheng Wang, Hui Zhang, and Zhengru Zhang. A positivity-preserving, energy stable and convergent numerical scheme for the cahn–hilliard equation with a flory–huggins–degennes energy. *Communications in Mathematical Sciences*, 17(4):921–939, 2019.

[18] Suchuan Dong and Jie Shen. A time-stepping scheme involving constant coefficient matrices for phase-field simulations of two-phase incompressible flows with large density ratios. *Journal of Computational Physics*, 231(17):5788–5804, 2012.

[19] Suchuan Dong and Jie Shen. A time-stepping scheme involving constant coefficient matrices for phase-field simulations of two-phase incompressible flows with large density ratios. *Journal of Computational Physics*, 231(17):5788–5804, 2012.

[20] Charles M Elliott. The cahn-hilliard model for the kinetics of phase separation. In *Mathematical models for phase change problems*, pages 35–73. Springer, 1989.

[21] Charles M Elliott and Donald A French. A nonconforming finite-element method for the two-dimensional cahn–hilliard equation. *SIAM Journal on Numerical Analysis*, 26(4):884–903, 1989.

[22] Charles M Elliott and Harald Garcke. On the cahn–hilliard equation with degenerate mobility. *Siam journal on mathematical analysis*, 27 (2):404–423, 1996.

[23] David J Eyre. Unconditionally gradient stable time marching the cahn-hilliard equation. *MRS online proceedings library (OPL)*, 529:39, 1998.

[24] Xiaobing Feng and Andreas Prohl. Error analysis of a mixed finite element method for the cahn-hilliard equation. *Numerische Mathematik*, 99:47–84, 2004.

[25] Florian Frank, Andreas Rupp, and Dmitri Kuzmin. Bound-preserving flux limiting schemes for dg discretizations of conservation laws with applications to the cahn–hilliard equation. *Computer Methods in Applied Mechanics and Engineering*, 359:112665, 2020.

[26] Daisuke Furihata. A stable and conservative finite difference scheme for the cahn-hilliard equation. *Numerische Mathematik*, 87(4):675–699, 2001.

[27] Jason Goulding, Mehrnaz Ayazi, Tamar Shinar, and Craig Schroeder. Simplified conservative discretization of the cahn-hilliard-navier-stokes equations. *Journal of Computational Physics*, 519:113382, 2024. ISSN 0021-9991. doi: https://doi.org/10.1016/j.jcp.2024.113382. URL https://www.sciencedirect.com/science/article/pii/S0021999124006302.

[28] László Gránásy and David W Oxtoby. Cahn–hilliard theory with triple-parabolic free energy. i. nucleation and growth of a stable crystalline phase. *The Journal of Chemical Physics*, 112(5):2399–2409, 2000.

[29] J.-L. Guermond and L. Quartapelle. A projection fem for variable density incompressible flows. *Journal of Computational Physics*, 165(1):167–188, 2000. ISSN 0021-9991. doi: https://doi.org/10.1006/jcph.2000.6609. URL https://www.sciencedirect.com/science/article/pii/S0021999100966099.

[30] Zhenlin Guo, Ping Lin, J Lowengrub, and Steven M Wise. Mass conservative and energy stable finite difference methods for the quasi-incompressible navier–stokes–cahn–hilliard system: Primitive variable and projection-type schemes. *Computer Methods in Applied Mechanics and Engineering*, 326:144–174, 2017.

[31] Qiaolin He, Roland Glowinski, and Xiao-Ping Wang. A least-squares/finite element method for the numerical solution of the navier–stokes-cahn–hilliard system modeling the motion of the contact line. *Journal of computational physics*, 230(12):4991–5009, 2011.

[32] Yinnian He, Yunxian Liu, and Tao Tang. On large time-stepping methods for the cahn–hilliard equation. *Applied Numerical Mathematics*, 57(5-7):616–628, 2007.

[33] Pierre C Hohenberg and Bertrand I Halperin. Theory of dynamic critical phenomena. *Reviews of Modern Physics*, 49(3):435, 1977.

[34] Qiong-Ao Huang, Wei Jiang, Jerry Zhijian Yang, and Cheng Yuan. A structure-preserving, upwind-sav scheme for the degenerate cahn–hilliard equation with applications to simulating surface diffusion. *Journal of Scientific Computing*, 97(3):64, 2023.

[35] Ziyang Huang, Guang Lin, and Arezoo M Ardekani. Consistent and conservative scheme for incompressible two-phase flows using the conservative allen-cahn model. *Journal of Computational Physics*, 420:109718, 2020.

[36] Ziyang Huang, Guang Lin, and Arezoo M. Ardekani. Consistent, essentially conservative and balanced-force phase-field method to model incompressible two-phase flows. *Journal of Computational Physics*, 406:109192, 2020. ISSN 0021-9991. doi: https://doi.org/10.1016/j.jcp.2019.109192. URL https://www.sciencedirect.com/science/article/pii/S0021999119308976.

[37] Ziyang Huang, Guang Lin, and Arezoo M Ardekani. A consistent and conservative volume distribution algorithm and its applications to multiphase flows using phase-field models. *International Journal of Multiphase Flow*, 142:103727, 2021.

[38] David Jacqmin. Calculation of two-phase navier–stokes flows using phase-field modeling. *Journal of Computational Physics*, 155(1):96–127, 1999. ISSN 0021-9991. doi: https://doi.org/10.1006/jcph.1999.6332. URL https://www.sciencedirect.com/science/article/pii/S0021999199963325.

[39] Guang-Shan Jiang and Chi-Wang Shu. Efficient implementation of weighted eno schemes. *Journal of computational physics*, 126(1): 202–228, 1996.

[40] Junseok Kim. A continuous surface tension force formulation for diffuse-interface models. *Journal of computational physics*, 204(2): 784–804, 2005.

[41] Dongsun Lee, Joo-Youl Huh, Darae Jeong, Jaemin Shin, Ana Yun, and Junseok Kim. Physical, mathematical, and numerical derivations of the cahn–hilliard equation. *Computational Materials Science*, 81:216–225, 2014.

[42] Xiao Li, ZhongHua Qiao, and Hui Zhang. An unconditionally energy stable finite difference scheme for a stochastic cahn-hilliard equation. *Science China Mathematics*, 59:1815–1834, 2016.

[43] Yibao Li, Hyun Geun Lee, Binhu Xia, and Junseok Kim. A compact fourth-order finite difference scheme for the three-dimensional cahn–hilliard equation. *Computer Physics Communications*, 200:108–116, 2016.

[44] Chen Liu, Deep Ray, Christopher Thiele, Lu Lin, and Beatrice Riviere. A pressure-correction and bound-preserving discretization of the phase-field method for variable density two-phase flows. *Journal of Computational Physics*, 449:110769, 2022.

[45] Chun Liu and Jie Shen. A phase field model for the mixture of two incompressible fluids and its approximation by a fourier-spectral method. *Physica D: Nonlinear Phenomena*, 179(3-4):211–228, 2003.

[46] JC Martin and WJ Moyce. An experimental study of the collapse of fluid columns on a rigid horizontal plane, in a medium of lower, but comparable, density. 5. *Philosophical Transactions of the Royal Society of London Series A-Mathematical and Physical Sciences*, 244(882): 325–334, 1952.

[47] Alain Miranville and Sergey Zelik. Robust exponential attractors for cahn-hilliard type equations with singular potentials. *Mathematical methods in the applied sciences*, 27(5):545–582, 2004.

[48] Shahab Mirjalili, Christopher B Ivey, and Ali Mani. A conservative diffuse interface method for two-phase flows with provable boundedness properties. *Journal of Computational Physics*, 401:109006, 2020.

[49] Rayleigh. Investigation of the Character of the Equilibrium of an Incompressible Heavy Fluid of Variable Density*. *Proceedings of the London Mathematical Society*, s1-14(1):170–177, 11 1882. ISSN 0024-6115. doi: 10.1112/plms/s1-14.1.170. URL `https://doi.org/10.1112/plms/s1-14.1.170`.

[50] Jie Shen and Xiaofeng Yang. Energy stable schemes for cahn-hilliard phase-field model of two-phase incompressible flows. *Chinese Annals of Mathematics, Series B*, 31(5):743–758, 2010.

[51] Jie Shen and Xiaofeng Yang. A phase-field model and its numerical approximation for two-phase incompressible flows with different densities and viscosities. *SIAM Journal on Scientific Computing*, 32(3):1159–1179, 2010.

[52] Garth N Wells, Ellen Kuhl, and Krishna Garikipati. A discontinuous galerkin method for the cahn–hilliard equation. *Journal of Computational Physics*, 218(2):860–877, 2006.

[53] Xiaofeng Yang and Jia Zhao. On linear and unconditionally energy stable algorithms for variable mobility cahn-hilliard type equation with logarithmic flory-huggins potential. *arXiv preprint arXiv:1701.07410*, 2017.

[54] Jun Zhang and Xiaofeng Yang. Non-iterative, unconditionally energy stable and large time-stepping method for the cahn-hilliard phase-field model with flory-huggins-de gennes free energy. *Advances in Computational Mathematics*, 46:1–27, 2020.

[55] Jingzhi Zhu, Long-Qing Chen, Jie Shen, and Veena Tikare. Coarsening kinetics from a variable-mobility cahn-hilliard equation: Application of a semi-implicit fourier spectral method. *Physical Review E*, 60(4):3564, 1999.